

@2011

Tao Ma

ALL RIGHTS RESERVED

**Macro-3D Carbon Nanotube/metallic Wool Hierarchical Hybrids
for Adsorptive Cooling and Novel TiO₂/graphene Composites
for Photocatalytic Applications**

by

Tao Ma

A Dissertation submitted to the

Graduate School-Newark

Rutgers, The State University of New Jersey

in partial fulfillment of the requirements

for the degree of

Master of Science

Graduate Program in Department of Chemistry

written under the direction of

Professor Huixin He

and approved by

Newark, New Jersey

Oct, 2012

ABSTRACT OF THE DISSERTATION

Macro-3D Carbon Nanotube/metallic Wool Hierarchical Hybrids for Adsorptive Cooling and Novel TiO₂/graphene Composites for Photocatalytic Applications By Tao Ma

**Dissertation Director:
Huixin He**

The objective of the research is to develop an innovative approach for a rapid and mass production of macro-3D hierarchical porous hybrids for adsorptive cooling. The most innovative feature of this cooling system is the capability to utilize solar energy or any heat waste as the driving force, which is an energy-favored and environmental-friendly alternative to traditional cooling systems. The macro-3D hierarchical porous hybrids are used as the adsorbent in the cooling system and composed with vertically aligned carbon nanotubes directly grown on highly conductive metal microwires in stainless steel wool. The stainless steel wool has stochastic foam features composed of microwires and pores of wide range of sizes from millimeters down to nanometers. Significantly improved performance for adsorptive cooling by this novel design is expected due to the unique 3D hierarchical porous structures, which not only dramatically increases effective surface area for coolant adsorption and desorption, but also facilitates mass transport of the coolants. Directly growing CNTs on a conductive surface will dramatically improve the contact between the CNTs and the underlying metal substrates, which has been a long-lasting problem and is the key to speed up heat transfer. To reach these goals, several important parameters, such as in-situ catalyst fabrication, growing temperature, flow rates of carbon

resources, reduction and inert carrier gases, were systematically investigated and optimized to grow vertically aligned carbon nanotubes on each metal wire in stainless steel wool. We also have established an adsorptive cooling system to study the cooling cycles using pressure-temperature (P-T) diagram. This system allows us to timely evaluate the refrigeration performance (such as the coefficient of performance, COP) of the fabricated novel 3D hierarchical porous adsorbent.

Another part of this thesis is to fabricate urchin-like or flower-like assembled TiO_2 nanorods/graphene nanocomposites by a facile hydrothermal treatment using an inorganic titanium source and highly-conductive, low-defective amphiphilic graphene sheets prepared by a microwave-enabled dispersion approach developed by our group. The structures and composition of the flower shaped composite particles and sheets were characterized by scanning electron microscope (SEM), Raman, and ultraviolet visible spectroscopy (UV-Vis), etc. The efficiency enhancement for photocatalytic reduction of CO_2 and photocatalytic oxidation of pharmaceutical drug waste in the environment will be examined in future studies.

Acknowledgements

First of all, I would like to show my sincere thanks to my supervisor Professor Huixin He for her long-term support and directions she has given me, which made it possible for me to accomplish this academic level. Her wealth of knowledge in nanomaterials and her patience allow me to discuss with her any problems I had in my projects.

I am also grateful to Dr. Roman Brukh for his assistance in the design and establishment of our experimental setup during the entire period of my laboratory work, and also his valuable advice to improve our system and experiment procedures.

My gratitude also goes to all my group colleagues, Pui Lam Chiu, Min Jeong, Ruiming Huang, Rishi Parajuli, Hsin-I Yen and William Cheung, for all of their assistance and teaching me all the techniques required in our lab. I especially thank Pui and Min for their conversations with me whenever I was stressful and moody; I will remember your kindness and our friendship forever.

I greatly appreciate Prof. Piotr Piotrowiak and Prof. Roger Lalancette for accepting me as a teaching assistant during the past two years. I have learned a lot from your advice and knowledge in my research and teaching job. Thank you also for offering me the chance to learn from you as being my committee members.

Finally, I am also grateful for my parents in China for their understanding and long-distance encouragement while I complete my thesis.

Table of Contents

Abstract.....	ii
Acknowledgements.....	iv
List of Figures.....	vii
List of Tables.....	ix
Chapter One: Introduction.....	1
1.1 Basics of CNTs.....	2
1.2 CNT Synthesis.....	4
1.2.1 Arc-discharge.....	4
1.2.2 Laser-ablation.....	5
1.2.3 Chemical Vapor Deposition.....	5
1.3 Material Properties of CNTs.....	7
1.4 Applications Based on CNTs	10
1.5 Adsorptive Cooling Fundamental and Technologies.....	13
1.5.1 Basic Adsorption Cycle.....	13
1.5.2 Performance Prediction of Adsorptive Cooling Cycle.....	16
1.5.3 Adsorption System Development.....	17
1.6 Novel Nanostructured TiO ₂ /Graphene Composites for Photocatalysis.....	20
1.6.1 Overview of TiO ₂ and Graphene.....	20
1.6.2 TiO ₂ Based Composites in Photocatalysis.....	21
References.....	22
Chapter Two:	
2.1 Synthesis of CNTs on Metallic Substrate by CVD.....	25
2.1.1 Materials and Instruments.....	25
2.1.2 Experimental.....	25
2.1.3 Results and Discussion.....	27
2.2 Adsorptive Heat Transformation Study for Solid Adsorbents.....	35

2.2.1 Materials and Instruments.....	35
2.2.2 Experimental.....	35
2.2.3 Results and Discussion.....	37
References.....	44

Chapter Three:

Synthesis of TiO ₂ Nanorods/graphene Composite Photocatalysts.....	45
3.1 Materials and Instruments.....	45
3.2 Experimental.....	45
3.3 Results and Discussion.....	46
3.3.1 Morphology of TiO ₂ Nanorods/Graphene Composites.....	46
3.3.2 Structure and Optical Properties of TiO ₂ Nanorods/Graphene.....	49
3.3.3 Mechanism Study of TiO ₂ Nanorods/Graphene Composites.....	51
References.....	53

Conclusion and Future Work.....	54
--	-----------

Curriculum Vitae.....	55
------------------------------	-----------

List of Figures

Fig.1.1 schematic illustration for different carbon based materials.....	1
Fig.1.2 Chiral vector and angle for a (2,4) tube on a graphene sheet.....	1
Fig.1.3 Three possible carbon nanotube atomic structures.....	1
Fig.1.4 Experimental setup of an arc-discharge apparatus.....	4
Fig.1.5 Schematic drawing of the laser ablation process.....	5
Fig.1.6 Schematic diagram of CVD setup in its simplest form.....	6
Fig.1.7 Two growth mechanisms for CNTs.....	7
Fig.1.8 Stress – strain response of a carbon nanotube under tensile loading.....	8
Fig.1.9 Tight binding calculated DOS versus energy for CNTs.....	9
Fig.1.10 Temperature dependence of thermal conductivity of a single bundle of SWCNTs.....	10
Fig.1.11 SEM image of the smallest CNTs/nylon working gear.....	11
Fig.1.12 Schematic representation of CNTFETs.....	12
Fig.1.13 Basic operation cycle for a single effect absorption chiller.....	14
Fig.1.14 Scheme of adsorptive cooling device.....	15
Fig.1.15 Typical adsorption cycle Clapeyron type diagram.....	15
Fig.1.16 Adsorption refrigerator invented by a) Monma and Mizota, and b) Patzner.....	18
Fig.1.17 Multi-stage, multi-adsorber adsorption refrigerator.....	18
Fig.1.18 The sketch structure of the no valve solar ice maker.....	19
Fig.2.1 Schematic illustration for CVD growth of CNTs.....	26
Fig.2.2 SS wool before and after CNT deposition.....	27
Fig.2.3 CNTs synthesized at various deposition temperatures.....	28
Fig.2.4 Relative weight gain of CNTs with respect to deposition temperature.....	29
Fig.2.5 SEM micrograph of CNT “seeds” on top of the metallic catalysts.....	29
Fig.2.6 SS wool substrate treated with HCl (~38%) for different times.....	30
Fig.2.7 SEM images of CNTs grown on SS316L with different preheating temperatures.....	32

Fig.2.8 SS wool conditioned at 700°C (HCl treated).....	33
Fig.2.9 Vertically aligned CNT forest at optimized condition.....	34
Fig.2.10 Scheme of experimental setup for NH ₃ sorption isosteres measurement.....	36
Fig.2.11 A photograph of realistic setup in the lab.....	36
Fig.2.12 A typical adsorption-desorption cycle for BaCl ₂ -NH ₃ working pair.....	38
Fig.2.13 Isosters of ammonia sorption on BaCl ₂ /vermiculite composite.....	39
Fig.2.14 Isosters of ammonia sorption on SWCNTs and MWCNTs.....	41
Fig.2.15 P-T diagram of NH ₃ adsorption-desorption on (a) SWCNTs, (b) MWCNTs.....	43
Fig.3.1 Procedure for hydrothermal synthesis of TiO ₂ nanorods/graphene composites.....	46
Fig.3.2 SEM images of TiO ₂ /graphene composites.....	47
Fig.3.3 SEM images of TiO ₂ nanorods/graphene synthesized with different reaction time.....	48
Fig.3.4 Raman spectroscopy of TiO ₂ nanorods/graphene composites.....	49
Fig.3.5 Raman Spectra of TiO ₂ nanorods/graphene with different graphene content.....	50
Fig.3.6 UV-vis adsorption spectra of pure TiO ₂ and TiO ₂ /graphene composites.....	50
Fig.3.7 Schematic illustration of the formation of 3D hierarchical TiO ₂ /graphene....	51

List of Tables

Table 2.1 Chemical Composition of Austenitic Stainless Steel (Type 316L).....	26
Table 2.2 CNT synthesis with different deposition temperatures.....	27
Table 2.3 Enthalpy and entropy of ammonia sorption on BaCl ₂ /vermiculite, SWCNTs and MWCNTs.....	41
Table 2.4 NH ₃ adsorption capacity calculation for different adsorbents.....	42

Chapter One

1.Introduction

Since the discovery of carbon nanotubes (CNTs) by Ijima [1], their fascinating electrical, mechanical and thermal properties have led them to numerous applications as device components, such as sensors [2], fuel cells [3-4], transistors [5] and many other energy related fields.

Among several techniques available to produce CNTs today, chemical vapor deposition (CVD) is the most popular approach. In this process, the carbon precursor, which is usually hydrocarbon vapor, experiences thermal decomposition in the presence of metal catalysts. This method is prevalent nowadays due to its low cost, high yield, and ease for scale-up in industry. Structurally, their high surface area, hollow and layered structures make them ideal adsorption materials [6]. In addition, carbon nanotubes are excellent conductors of heat, at about $3000\text{W}/(\text{m.K})$ for multiwall carbon nanotubes (MWCNTs) and about $6600\text{W}/(\text{m.K})$ for single walled carbon nanotubes (SWCNTs). [7, 8] Therefore, carbon nanotubes become good candidates as solid refrigerants for adsorptive cooling systems, which appears to be an attractive alternative for cooling or air conditioning-related applications.

Graphene is another allotrope of carbon with unique electronic and structural properties, suggesting that it has great potential to enhance the photocatalytic activity of catalysts such as TiO_2 . Some novel nanostructured TiO_2 /graphene composites have been fabricated by hydrothermal, sol-gel methods. In addition, recent advances in solution-phase separation of graphene from graphite further expedite the study and application in photocatalytic nanocomposites.

1.1 Basics of CNTs

Carbon nanotubes can be considered as cylindrical allotropes of carbon, where sheets of graphite (called graphene sheets) have been rolled-up into a tube [9].

Depending on the number of graphene sheets, CNTs can be divided into two categories: single walled carbon nanotubes (SWCNTs) and multi-walled carbon nanotubes (MWCNTs). SWCNTs are carbon cylinders with only one layer of graphene sheet. By changing the direction in the roll-up, carbon nanotubes can be produced with different chiralities [10]. It is also possible that several tubes of different diameters can be fitted into one another to produce multi-walled carbon nanotubes, as shown in Fig. 1.1 [11].

Based on the orientation of the horizontal cells, carbon nanotubes have three forms: zigzag, armchair and chiral. They are generally described by a single chiral vector which is defined by the relation:

$$\vec{C} = n\vec{a}_1 + m\vec{a}_2 \quad (1)$$

where n and m are integers, \vec{a}_1 and \vec{a}_2 are unit cell vectors (Fig. 1.2). The length of the chiral vector \vec{C} is the circumference of the nanotube, which is given by

$$c = |\vec{C}| = a\sqrt{n^2 + nm + m^2} \quad (2)$$

where a is the length of the unit cell vector. The angle between the chiral vector and zigzag nanotube axis is the chiral angle θ . Those three forms of CNTs mentioned before can be revealed by the pairs of integers (n, m) : when $m=0$, it is zigzag type; when $n=m$, it is called armchair type; otherwise ($n \neq m$), it is chiral.

The value of (n, m) determines the chirality and affects the mechanical, optical and electronic properties. These structures are shown in Fig.1.3. Nanotubes with $|n - m| = 3q$ are metallic and those with $|n - m| = 3q \pm 1$ are semiconductor (q is an integer) [12].

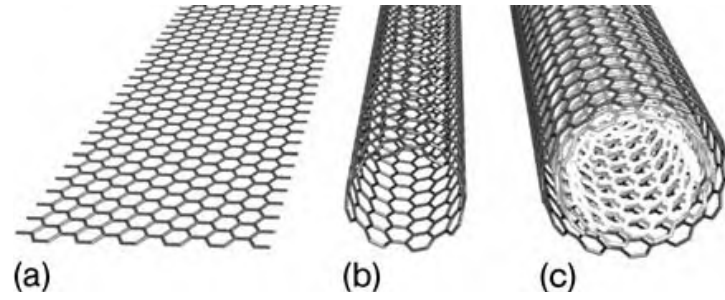


Fig.1.1 schematic illustration for different carbon based materials
 (a) structure of a single layer of graphite (graphene); (b) single walled carbon nanotube; (c) multi-walled carbon nanotube with three shells [11].

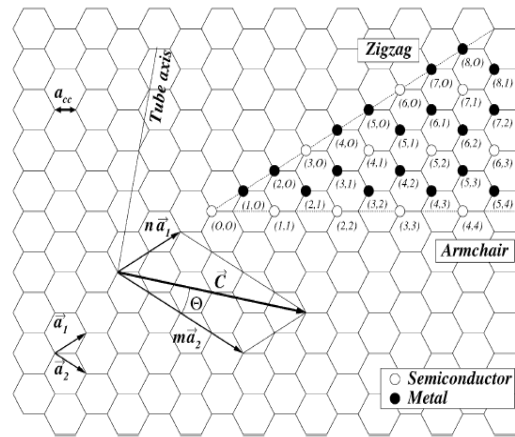


Fig. 1.2 Chiral vector \vec{C} and angle θ for a (2,4) tube on a graphene sheet. \vec{a}_1 and \vec{a}_2 are unit cell vector. θ is defined as the angle between chiral vector and zigzag nanotube axis [12].

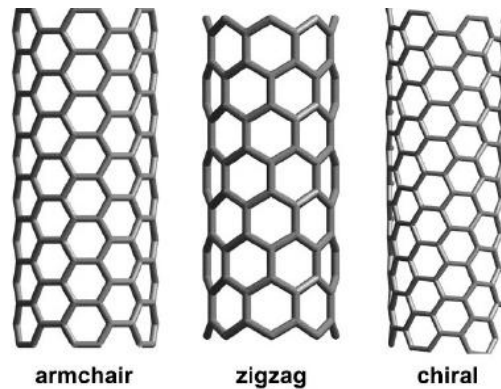


Fig.1.3 Three possible carbon nanotube atomic structures [12].

1.2 CNT Synthesis

Since the early 1990s, when Ijima synthesized CNTs for the first time, multiple methods have been developed to produce CNTs. The primary methods to produce CNTs nowadays are arc-discharge, laser ablation and chemical vapor deposition. Different production methods and specific growth parameters can result in a plethora of CNT structures.

1.2.1 Arc-discharge

The carbon arc-discharge method, initially used for C_{60} fullerenes synthesis, is the most practical and probably the easiest way to produce CNTs as it is simple to undertake. This method creates CNTs in an inert atmosphere by applying a voltage to two high-purity graphite rods, which act as an anode and a cathode. Once the arc is achieved, it strips carbon atoms off from the anode and deposit them on the cathode to form CNTs and other carbon particles. Two distinct methods of synthesis can be performed in arc-discharge apparatus as shown in Fig. 1.4 [13]. Arc discharge method yields highly graphitized tubes due to its sufficient high processing temperature and it is possible to selectively grow SWCNTs or MWCNTs.

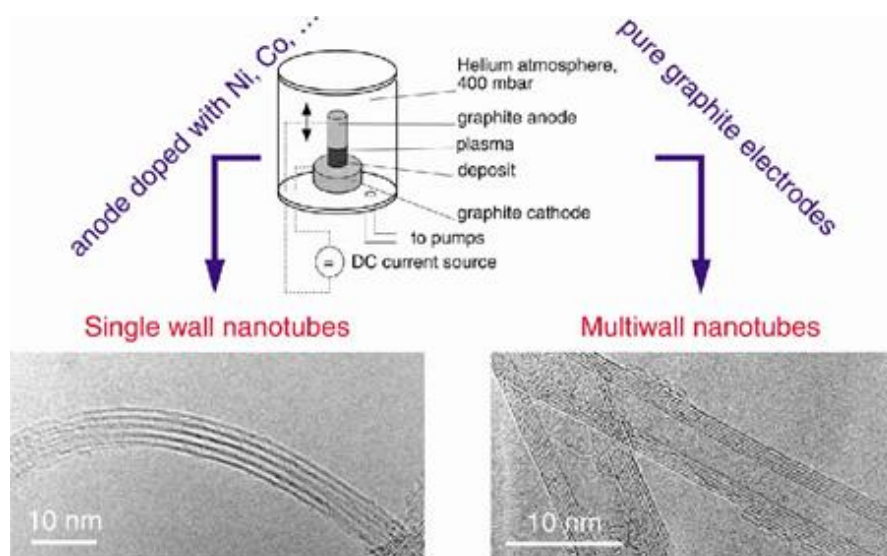


Fig.1.4 Experimental setup of an arc-discharge apparatus [13].

1.2.2 Laser Ablation

The laser ablation method utilizes a pulsed [14], or continuous [15] laser to vaporize a graphite target in a heated oven at about 1200°C with flowing helium or argon gas. Usually a mixture of Co and Ni were used to catalyze the carbon vapor to CNTs [16], and a typical process is shown in Fig. 1.5.

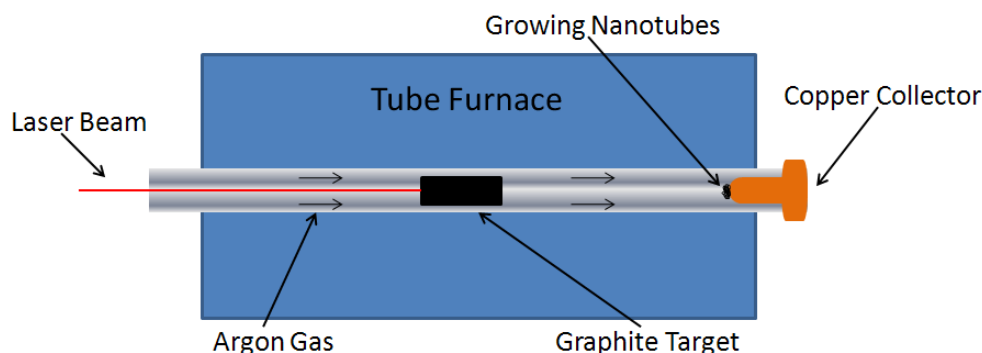


Fig. 1.5 Schematic drawing of the laser ablation process [16].

Laser ablation is similar to arc discharge because the carrier gas and catalyst are almost the same, and the reaction may occur by the same or at least similar mechanism.

Due to this similarity, both arc discharge and laser ablation approaches suffer from the same primary drawbacks. They are difficult to be scaled up for industrial applications and undesirable particles like junk carbon are always mixed with tangled CNTs, so additional purification steps are required to extract pure CNTs for practical applications. These limitations have led to the development and prevalence of chemical vapor deposition method, which is a simple and economic technique.

1.2.3 Chemical Vapor Deposition (CVD)

In a typical chemical vapor deposition method, hydrocarbon gas goes through a tubular reactor where the catalytic material is present at sufficient high temperature. Once the carbon source has been cracked into active carbon atoms,

they diffuse toward the substrate coated with a thin layer of catalyst where it will bind. Usually the catalyst is the nanoparticles made from the first row transition metal such as Ni, Fe or Co. This process is illustrated in Fig. 1.6 [16].

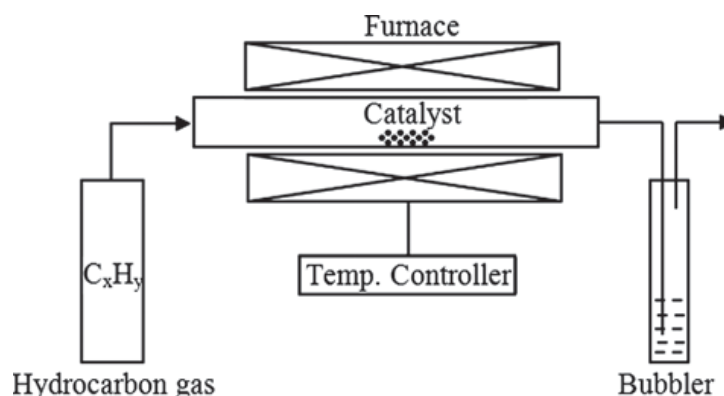


Fig. 1.6 Schematic diagram of CVD setup in its simplest form [16].

During CNT growth, the carbon vapor comes into contact with metal particles and decomposes into active carbon species which dissolve into the catalyst. Once reaching the carbon solubility limit, excess carbon species begin to precipitate out and crystallize in the form of CNTs. There are two general accepted mechanisms. When the catalyst-substrate interaction is weak, hydrocarbon decomposes on the top of the metal particles and diffuses down through the metal, and CNTs precipitate out on the bottom of the catalyst, pushing the whole metal particle off the substrate. This growth process will continue until the metal catalyst is not available for carbon decomposition. This is known as tip growth model [17].

In the other case, hydrocarbon initially decomposes and diffuses in a similar way as the tip growth model, but the catalyst-substrate interaction is much stronger so that CNT precipitation fails to push the metal particles up. Hence, CNTs emerge out from the metal particle apex, which then extend up to form graphite cylinders. This is known as base growth model [18]. Both mechanisms are illustrated in Fig. 1.7.

CVD is versatile in the sense that it allows CNT structure architecture with

high yield and purity. It offers better control on the growth parameters such as species of hydrocarbons in any state (solid, liquid or gas), deposition temperature, flow rate, growth time and substrate properties.

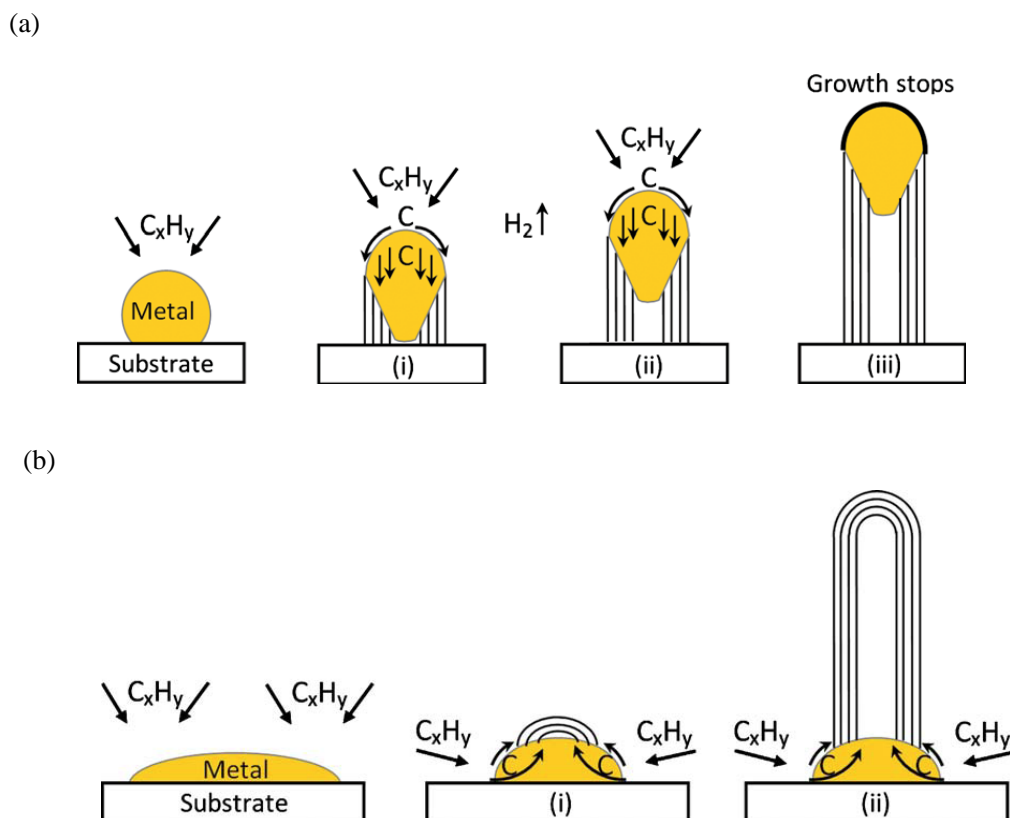


Fig.1.7 Two mechanisms for CNTs: (a) tip-growth model, (b) base-growth model [16].

1.3 Material Properties of Carbon Nanotube

Scientific research interest in CNTs is sparked by their unique mechanical, electrical and thermal properties. Both theoretical and experimental studies are performed to evaluate and explore their properties.

Mechanically, CNTs have remarkably high strength and elastic modulus, as well as significant flexibility and ductility and therefore they can withstand high longitudinal strain and bending moments. The Young Modulus can exceed 1TPa [19] in the axial direction (usually 230GPa for stainless steel). The stress-strain response of armchair and zigzag CNTs under tensile loading are illustrated in Fig. 1.8. In contrast, CNTs can easily buckle under compression or appropriate

pressure as result of the high flexibility. The mechanical behavior of CNT has created great interest in their use as structural materials. For instance, CNTs are ideal additives in material matrix as reinforcing fibers. The mechanical behaviors of CNTs are further elucidated in a previous review [20]. Their response to deformation at elastic regime, the behavior at large strains and the yield mechanism and strength at failure when bent are all challenging and active research fields at both the theoretical and experimental levels.

CNTs also have excellent electronic conductivity in the axial direction. When the graphene sheet is rolled to the cylindrical structure of SWNT, the π and π^* electron clouds experience significant curvature, which causes partial $\sigma - \pi$ hybridization. This leads to a 1D quantum-confinement structure, where the density of states (DOS) shows strong dependence on nanotube diameter, chirality, and type (metallic vs. semiconducting), as shown in Figure 1.9 [21].

Many theoretical calculations showed that the electronic properties of the CNTs are very sensitive to their geometric structure. This sensitivity of the electronic properties of CNTs to their structure is caused by the band-folding behavior of a graphene sheet. Also, as mentioned before, theoretical calculations also indicate that CNTs can be metals or semiconductors with different sized energy gaps, depending very sensitively on the diameter and helicity of the tubes, e.g. indices (n, m).

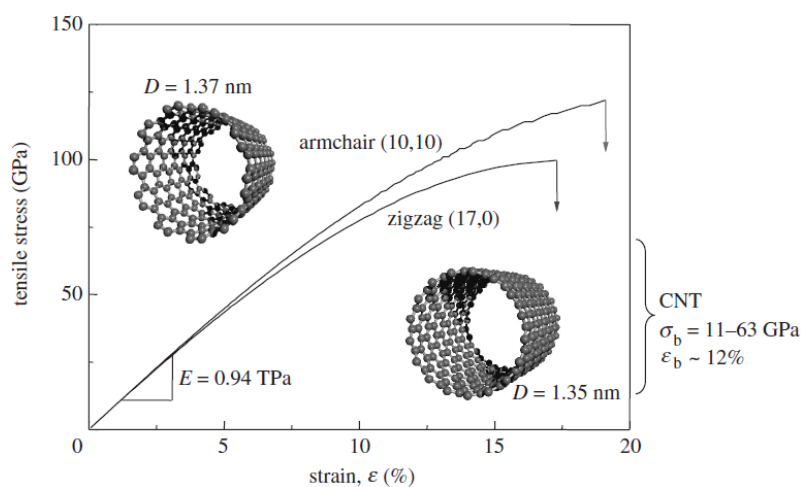


Fig. 1.8 Stress - strain response of a carbon nanotube under tensile loading

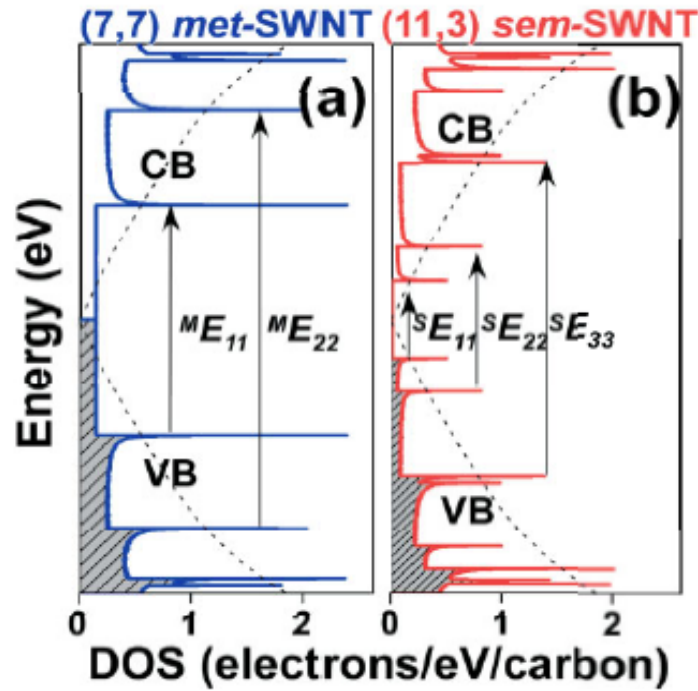


Fig. 1.9 Tight binding calculated DOS versus energy for

a) (7, 7) met- b) (11, 3) sem-SWNTs

(dotted curves indicate VB and CB of planar 2D graphene lattice)

Experimentally, research is focused on single-electron charging and resonant tunneling through the quantized energy levels of the nanotubes to understand the electronic properties [22]. The most prevalent technique is using scanning tunneling microscopy (STM) to directly probe the relationship structure and electronic properties of CNTs. As a result, the local density of states (LDOS) can be obtained to compare with the theoretical predictions [23]. Theoretical calculations of electrical current density range from 10^9 to 10^{13} A/cm², and experimentally a SWCNT has been measured to be 10^7 A/cm², almost 100 times greater than copper [24].

CNTs are also believed to have excellent thermal conductivity, and the theoretical predictions suggest the thermal conductivity could be as high as 3000-6600 Wm⁻¹K⁻¹ [7, 8]. However, the thermal behavior of SWNTs has not been as extensively studied experimentally as the electronic or mechanical properties.

The thermal conductivity κ of CNTs are dominated by low-frequency phonons and limited by their crystallite size. The thermal conductivity along the nanotube axis is determined by the kinetic formula as shown below [25]:

$$\kappa_z = \sum C v_z^2 \tau \quad (3)$$

where C , v and τ are specific heat, group velocity and relaxation time of a given phonon state, respectively. Measurements have been reported on thermal conductivity of CNT bundles, but the measured thermal conductivity is poorly correlated with the theoretical estimation, as shown in Fig. 1.10 [26]. This departure from a linear T dependence (which is actually $\sim T^{1.6}$ dependence)

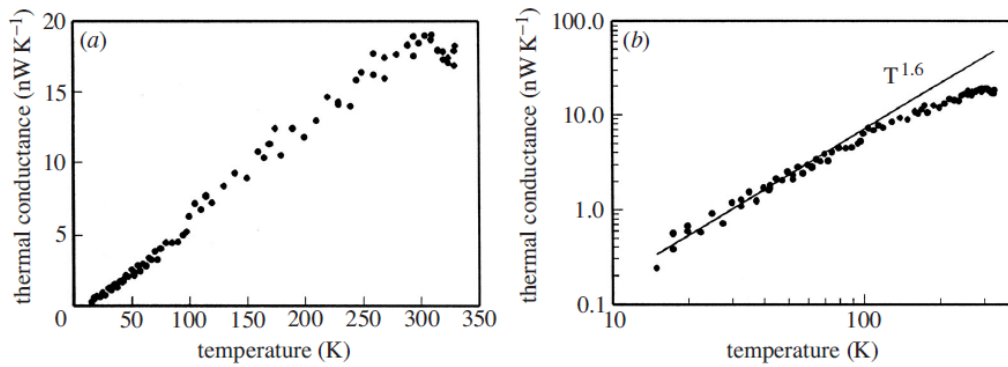


Fig. 1.10 Temperature dependence of thermal conductivity of a single bundle of SWCNTs

(a) Linear T plot, and (b) Log plot [26].

may be due to large resistances between neighboring tubes caused by coupling to optical phonons and intertube scattering/conduction processes [25]. The studies of single nanotubes will allow more detailed measurements of intertube contributions to thermal transport. The quantum thermal phenomena at low temperatures should be especially interesting regarding studies of the effect of individual selected phonons on the various thermal properties [26].

1.4 Applications based on CNTs

The size-dependent mechanical, electronic and thermal properties have resulted in thousands of proposed applications in a wide range of fields. Some of the applications have already been realized upon their unique structures and

properties.

The strong mechanical properties of CNTs have led to intensive studies of CNTs as additives for various matrices, especially polymers [27]. One of the best uses of this intrinsic property is the production of small working composite gears, which are obtained by mixing CNTs into molten nylon and then injecting into a tiny mold. This gear is as small as the diameter of a human hair, as shown in Fig. 1.11 [26].

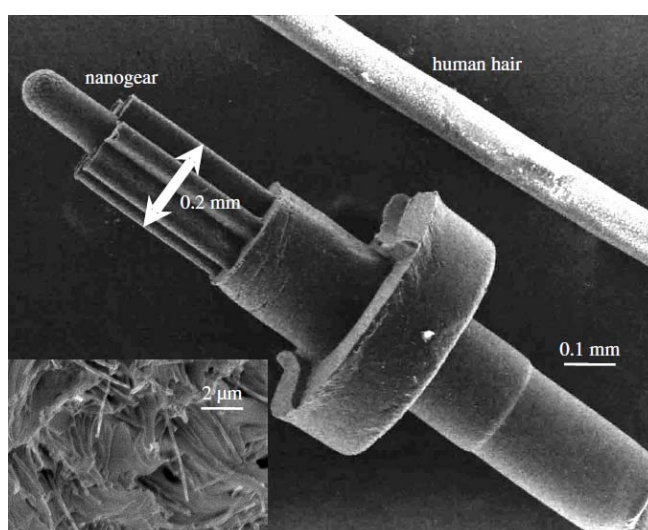


Fig. 1.11 SEM image of the smallest CNTs/nylon working gear [26].

(the inset shows the fractured surface)

The CNTs/nylon composites have remarkable improvement of the tensile strength, abrasion resistance and also electrical and thermal conductivity. The high tensile strength may allow CNTs to replace steel in many applications such as cables or reinforcement in concrete.

The unique network of carbon-carbon bonds and 1D quantum confinement properties of CNTs lead to great application potentials for micro and nano-scale electronic devices. CNTs are currently considered as promising building blocks of future nanoelectronics. The high conductivity and stability of metallic nanotubes make them excellent candidates for future use as interconnects in nanodevices and circuits [11, 28]. FETs using semiconducting CNTs have operating characteristics

that are as good as or better than state-of-the-art silicon devices, and significant improvements are expected in the near future. As shown in Fig.1.12 [29], SWCNTs

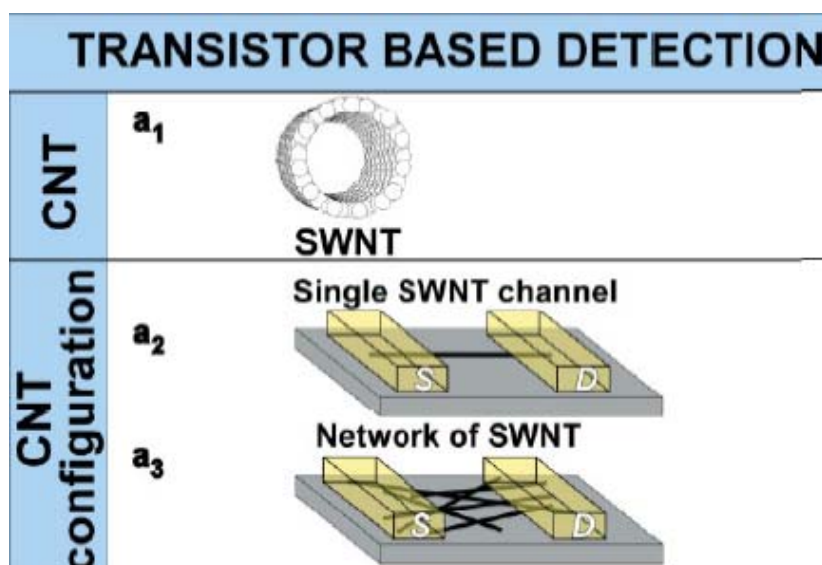


Fig. 1.12 Schematic representation of CNTFETs [29].

were used to bridge two noble metal electrodes which were previously fabricated by lithography on oxidized silicon wafer. SWCNTs were dispersed on the substrate and played the role of conductive “channel”, while the two metal electrodes are source and drain electrodes. The oxidized silicon wafer substrate was the gate. A further strong coupling of CNTs with metal such as Ti or Co fabricated on top of the devices was used to dramatically reduce the contact resistance between the carbon nanotubes and the metal electrodes. Overall, the possible applications of carbon nanotubes range from electronics to field emission displays, energy-storage devices and functional fillers in composites. These have attracted both industrial and academic interest. Therefore, it is important that some of the basic knowledge is transferred to industry very shortly so that practical and novel devices appear commercially.

In regard to thermal applications, SWCNTs can absorb the entire spectrum of solar energy with strong absorption capability from UV to visible and NIR region.

It is reported that the absorbed NIR light can be efficiently converted to heat. The remarkable capability in conversion of NIR light to heat has been exploited for selective photo-thermal ablation of cancer cells both in *vitro* and in *vivo*. Their large surface area, excellent thermal conductivity and remarkable capability in converting of NIR light to heat will be explored in this work to develop efficient and light adsorptive cooling systems.

1.5 Adsorptive Cooling: Fundamental and Technologies

Adsorptive cooling is a thermally driven cooling system, which can be powered by solar energy as well as waste heat produced by any running devices. The use of thermally driven systems helps to reduce the greenhouse gas (GHG, such as CO₂) emission into the environment. In addition, compared with conventional vapor compression systems, the adsorptive systems mainly use a natural working fluid such as water/ammonia, which is free of ozone depletion effect.

However, adsorptive cooling systems still can't replace traditional vapor compression systems in many applications due to several limitations, such as long adsorption/desorption time, low cooling efficiency, i.e., low Specific Cooling Power (SCP), low Coefficient of Performance (COP). To solve these problems, tremendous efforts have been made mainly focusing on the aspects of improving the adsorption/desorption cycle to recover more heat, modification of adsorbent bed to enhance heat and mass transfer, and development of novel adsorbent materials to improve adsorption/desorption cycle and COP [30-32].

1.5.1 Basic Adsorption Cycle

Instead of using mechanical energy, adsorptive chillers use heat to provide cooling. The principle is very similar to that of conventional liquid absorption cooling systems, in which the basic absorption chiller system includes the following components: absorber, generator, condenser and evaporator as shown in Fig. 1.13 [33]. The crucial differences between the liquid absorptive systems

are the heat and mass exchangers are now a fixed bed with solid/gas working pairs instead of liquid/gas working pairs. As a result, the thermodynamic properties of the adsorbent/refrigerant system are different from the adsorption systems, which require different cycle designs. In a typical adsorptive cooling system, adsorbent material is embedded and the scheme is presented in Fig. 1.14 [34].

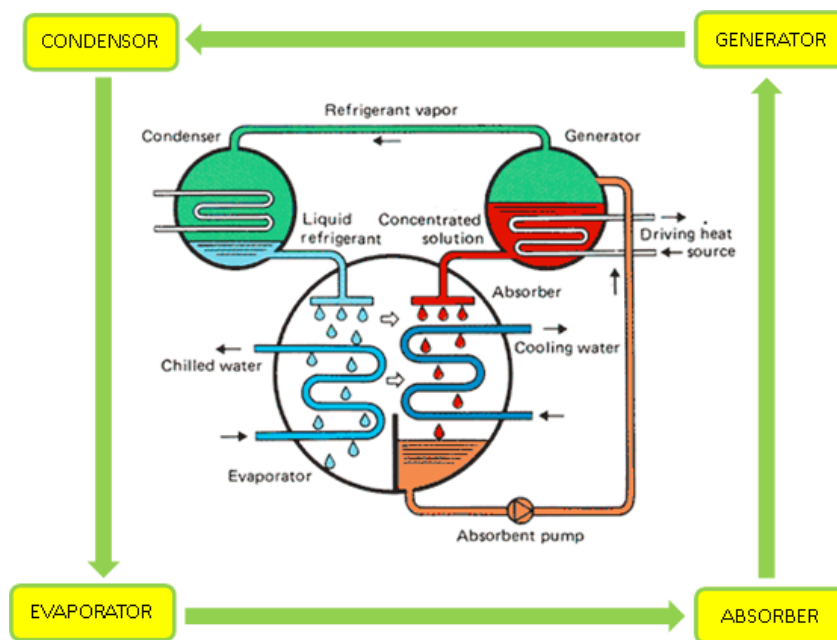


Fig. 1.13 Basic operation cycle for a single effect absorption chiller [33].

The basic cycle can be described as: (I) the energy from sun or waste heat received by the adsorbent bed leads to desorption of refrigerant gas from solid adsorbent materials, and then the desorbed refrigerant gas flows through the condenser and is condensed in the receiver. (II) After that, the valve V_1 is open to allow the liquid refrigerant to flow into the evaporator. (III) Then valve V_1 is closed and valve V_2 is open, allowing the liquid refrigerant to evaporate. The evaporated refrigerant gas flows to the adsorbent bed and adsorbs again on the adsorbent materials. The evaporation of refrigerant gas inside the cold chamber cools down the liquid water which then can be converted to ice.

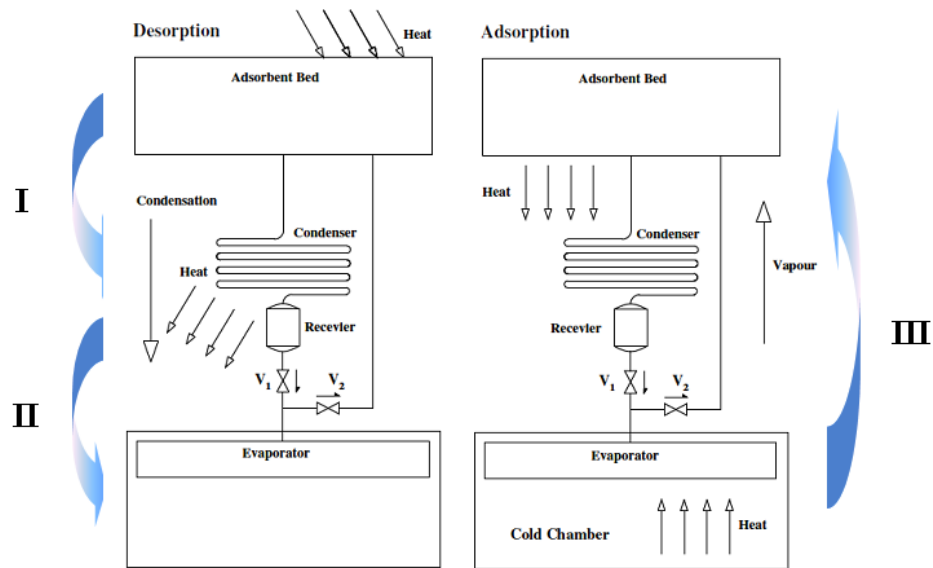


Fig. 1.14 Scheme of adsorptive cooling device. (I) desorption of refrigerant gas by solar energy or waste heat and condensing, (II) liquid refrigerant pass through into evaporator, (III) evaporation of liquid refrigerant and cooling is produced by readsorption of refrigerant gas [34].

From the thermodynamic point of view, the active refrigerant/adsorbent working pair follows the classic adsorptive cycle made of four phases, as shown in Fig. 1.15 [35]: (I) isosteric heating from p_{ev} to p_c (line AB); (II) isobaric desorption at high temperature and pressure of condensation (line BC); (III) isosteric cooling at closed volume from p_c to p_{ev} (line CD), where P_c and P_{ev} are condensing pressure and evaporation pressure, respectively; (IV) adsorption at low temperature and pressure of evaporation (line DA).

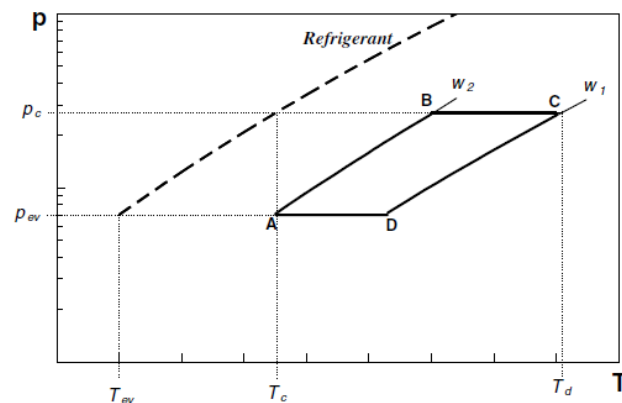


Fig. 1.15 Typical adsorption cycle Clapeyron type diagram [35].

1.5.2 Theoretical Prediction of the an Adsorptive Cooling Cycle Performance

An adsorptive cooling cycle is a three-temperature cycle. Compared to the vapor compression cooling system (two-temperature cycle), which requires mechanical energy, the adsorptive cooling cycle is mechanical energy free. The efficiency of adsorptive cooling can be defined through the cooling coefficient of performance (COP), which is the ratio of cooling load (heat output) to driving energy (heat input).

$$\text{COP} = \frac{Q_{\text{ev}}}{Q_{\text{h}}} \quad (4)$$

in which Q_{ev} and Q_{h} are the amount of heat released by the cooling cycle and the heat provided for driving the process, respectively. The three boundary temperatures are the temperature of the evaporator (T_{e}), condenser (T_{c}) and generator (T_{g}). The evaporator temperature is the temperature of cooling effect produced and it depends on the cooling device applied. The condenser temperature is close to the temperature of the ambient to which the heat produced during condensation should be released. It depends on climatic conditions of the device operation and usually lies in the range of 25 – 45°C. The generator temperature is determined by of the external heat source, which drives the cooling cycle [36]. These three temperatures are also illustrated in Fig.1.15 (where $T_{\text{g}}=T_{\text{d}}$ in Fig.1.15).

On the basis of an actual cooling cycle, the COP can be estimated as [36]

$$\text{COP} = \frac{Q_{\text{ev}}(w_{\text{max}} - w_{\text{min}})}{Q_{\text{des}}(w_{\text{max}} - w_{\text{min}}) + \left(\sum_i C_{\text{pi}} \omega_i + C_{\text{pr}} \omega_{\text{r}} \right) (T_{\text{g}} - T_{\text{c}})} \quad (5)$$

where Q_{ev} (J/g) is the heat of refrigerant gas evaporation, Q_{des} (J/g) is the isosteric heat of gas desorption, w_{max} and w_{min} are the gas uptakes corresponding to weak (line CD in Fig. 1.15) and rich isosters (line AB in Fig. 1.15) (g/g), C_{pi} is specific heat of component i in adsorbents and ω_i is the content of component i . C_{pr} is the specific heat of refrigerant gas and ω_{r} is the content of refrigerant gas which is permanently trapped in the adsorbents.

In ideal case, the adsorptive cooling can be considered as Carnot cycle, and

the Carnot COP was calculated as [38]

$$\text{COP}_{\text{Carnot}} = \frac{1 - T_c/T_g}{T_c/T_g - 1} \quad (6)$$

This is also the highest COP one can obtain with an ideal system. Usually the estimated COP for a realistic system is much smaller than Carnot COP. The major reason for such difference is the entropy generation due to the irreversibility of the heat transfer from an external heat source at the temperature T_g to the adsorber at temperature $T < T_g$ [37].

The specific cooling power (SCP) is evaluated as

$$\text{SCP} = \frac{Q_{\text{ev}}(w_{\text{max}} - w_{\text{min}})}{t_{\text{cycle}} \times m_{\text{adsorbent}}} \quad (7)$$

where t_{cycle} is the cycle time and $m_{\text{adsorbent}}$ is the mass of the adsorbent. Depending on different adsorptive cooling systems setup, the formula used for COP and SCP evaluation may have different forms.

1.5.3 Adsorption System Development

Novel adsorption systems are invented with different focuses. For one bed machine, simple structure and low cost are pursued. Several multi-bed systems are suggested to provide steady refrigeration and higher energy performance. In order to increase the system COP and SCP, various heat and mass recovery based on different adsorbent bed and different control strategies are disclosed [39]. No valve ice maker and heat pipe technologies are used to reduce components and simplify the system control, with the potential to enhance system performance. Fig.1.16(a) illustrates a typical one bed adsorption refrigerator invented by Monma and Mizota [40]. It contains a refrigeration chamber, an evaporator and an adsorbent bed. Detailed description of the device can be found in [40]. Patzer [41] developed a cooling system using zeolite as adsorbent, water as refrigerant, with an evaporator, as shown in Fig.1.16 (b).

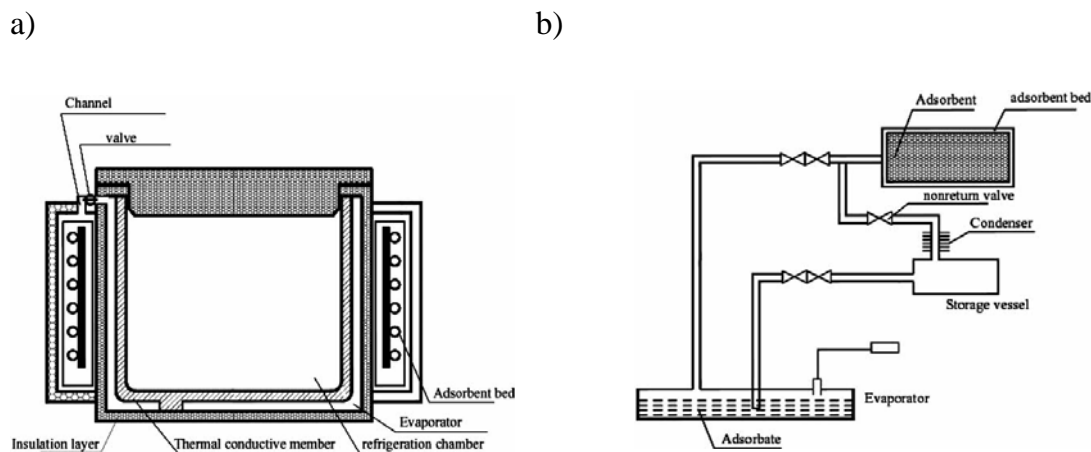


Fig.1.16 Adsorption refrigerator invented by a) Monma and Mizota [40], and b) Patzner [41].

The examples illustrated above are one bed systems, which only provide cooling intermittently, resulting in low COP and SCP. Therefore, two-bed or multi-bed systems are employed to improve the cooling efficiency. Sato et al. [38] have proposed a multi-stage multi-bed strategy involving cooling the adsorber with refrigerant emanating from one or more evaporators (Fig.1.17).

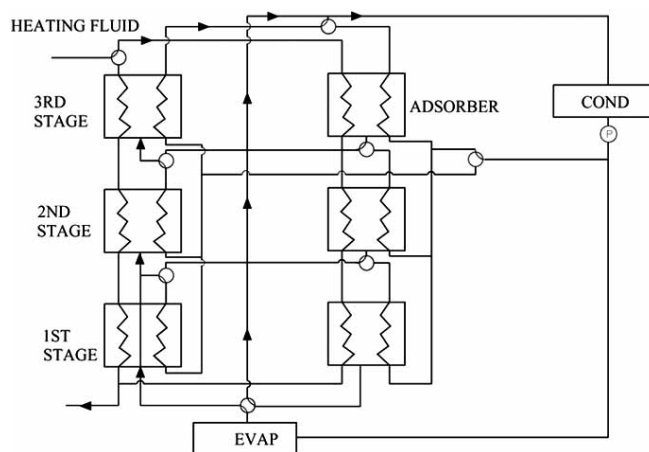


Fig.1.17 Multi-stage, multi-adsorber adsorption refrigerator

A no valve, flat plate solar ice maker is developed on the basis of previous research achievements of a large number experiments and theory analysis, as shown in Fig.1.18 [42].

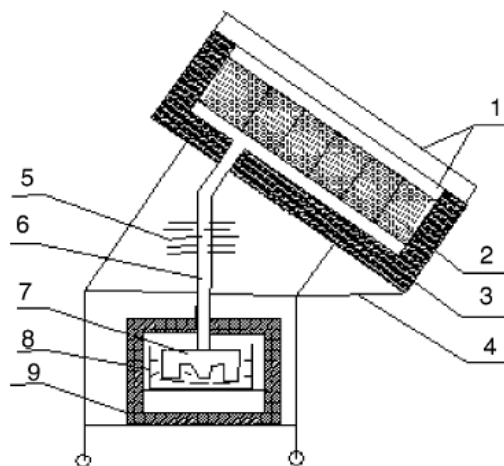


Fig.1.18 The sketch structure of the no valve solar ice maker: (1) cover plate, (2) adsorbent bed, (3) insulation materials, (4) ice frame, (5) condenser, (6) connecting pipe, (7) evaporator, (8) water tank, (9) insulation box [42].

For adsorption cooling system, significant achievements have been obtained on the use of various technologies to reduce the complexity of system structure, initial cost, to increase the system operation reliability as well as energy performance.

Adsorbent bed is the heart of the adsorption system. Heat and mass transfer between the adsorbent material and gas fluid are the most influential factors on adsorption cooling performance. Various adsorbent modules have been developed to obtain better heat transfer as well as to reduce the system manufacture complexity with different cooling capacities. Improving or applying the previous patented modules or developing new adsorbent module for novel systems is attractive to make adsorption system with flexible cooling capacity.

Based on traditional adsorbents, such as silica gel, zeolite, and activated carbon, modified or composite adsorbent materials were developed which achieve high adsorption capacity, better thermal conductivity and high permeability. Heat and mass transfer were largely improved in these composite adsorbents. However, the heat and mass transfer characteristics should be further enhanced in order to achieve a higher SCP for adsorption refrigeration system for practical applications[39].

In this thesis, we developed a convenient NH_3 sorption system which allows us to perform preliminary study on the thermodynamic properties of refrigerant gas-solid adsorbent working pairs in order to predict their adsorptive cooling efficiency. In future studies, we will set up a real cooling system to measure the cooling effect of different adsorbents including our stainless steel-CNT composites.

1.6 Novel nanostructured TiO_2 /Graphene composites for photocatalysis

With the advancement of nanoscience and nanotechnology, the fabrication of 2D or 3D hierarchical assembly of ordered nanostructures are becoming more and more interesting to scientists in various research fields. Due to the high surface area and related unique properties, materials with novel nanostructures are expected to have great potential to find applications in drug delivery, catalysis, electronic device manufacturing and magnetic recording [43-46].

1.6.1 Overview of TiO_2 and Graphene

As an important wide band gap semiconductor material, titanium oxide (TiO_2) has been extensively studied because of its several advantageous properties, such as chemical and biological inertness, nontoxicity under most conditions and low production cost [47]. TiO_2 exists in different crystalline forms known as anatase, rutile and brookite. Anatase and brookite are thermodynamically metastable and can be irreversibly converted to rutile form, especially at high temperature [48]. The size, crystallinity and morphology of TiO_2 play crucial roles in its properties and applications [47, 49-51]. In particular, TiO_2 has been demonstrated as excellent catalysts for photodegradation of organic contaminants or carbon dioxide (CO_2) reduction [52, 53]. Nanosized TiO_2 even has dramatically enhanced photocatalytic activity. TiO_2 nanotubes [54], hollow nanoparticles [55], nanofilm [56] and hierarchical flower-like or urchin-like nanostructures [57, 58] have been produced by various techniques, such as hydrothermal reaction, sol-gel process and electrochemical oxidation.

Graphene, a one-atom-thick planar sp^2 bonded graphite layer, is another allotrope of carbon besides fullerene (0D) and CNTs (1D). Due to the unique chemical and electronic properties, graphene has attracted considerable attention and has been studied extensively [59-62]. Graphene has even higher surface area compared with CNTs (estimated as $\sim 2630 \text{ m}^2/\text{g}$ in theory) and also a high electron mobility of $15000 \text{ m}^2 \text{ V}^{-1} \text{ s}^{-1}$ [63, 64], so it is expected to have better interfacial contact with adsorbates. Synthesizing composites by integrating graphene and other inorganic materials is the focus to expand their applications.

1.6.2 TiO₂-based Composites in Photocatalysis

During photocatalytic process, electrons in TiO₂ are excited from valence band (VB) to conduction band (CB), forming electron-hole pairs, which are responsible for photocatalytic activity. However, the excited electrons have a recombination rate in the order of 10^{-9} s, while the time required for the reaction between TiO₂ and most organic pollutants is around $10^{-8} \sim 10^{-3}$ s. Therefore, the lag between these two times limits the photocatalytic efficiency [65]. Scientists have made great efforts to fabricate TiO₂-based composites in order to hinder the electron-hole recombination and extend the photoresponse into the visible range, such as TiO₂/Au composites [64], CdS/TiO₂ hybrid [65] and carbon material doped TiO₂ [66].

Employing graphene as an electron acceptor in composites has been reported recently [63, 67]. When graphene is combined with TiO₂, the electrons can flow through the interface between graphene and TiO₂ due to their energy levels. The heterojunction formed at the interface (Schottky barrier) helps to further separate the photogenerated electron-hole pairs to prevent or at least slow down the charge recombination, which make it possible to realize higher photocatalytic efficiency and extend the photocatalysis to the visible range [67, 68]. It is still a great challenge to prepare TiO₂/graphene composites with controllable morphology and crystal structure to achieve dramatically enhanced photocatalytic activity.

References

- [1] S. Iijima, *Nature* 354 (1991), 56.
- [2] J. Kong, N.R. Franklin, C. Zhou, M.G. Chapline, S. Peng, H. Dai, *Science* 299 (2003) 1042.
- [3] Y. Chen, J. Wang, H. Liu, R. Li, X. Sun, S. Knights, *Electrochem. Commun.* 11 (2009) 2071.
- [4] M. Saha, R. Li, X. Sun, *J. Power Sources* 177 (2008) 314.
- [5] B. Kannan, J.H. Eduardo, W.R. Thomas, B. Marko, K. Klaus, *Organic Electronics* (2009) 567.
- [6] Y. M. Zhao, W. B. Hu, I. Ahmad, Y. Q. Zhu, X. J. Peng, Z. K. Luan, *J. Physics*, 61 (2007) 698.
- [7] J. Che, T. Cagin, W. A. Goddard, *Nanotechnology*, 11 (2000) 65.
- [8] S. Berber, Y. Kwon, D. Tomanek, *Phys. Rev. Lett.* 84 (2000) 4613.
- [9] E. Thostenson, Z. Ren, T. Chou, *Comp. Sci. Technol.* 61 (2001) 1899.
- [10] R. Seidel, G. S. Duesberg, E. Unger, A. P. Graham, M. Liebau, F. Kreupl, *J. Phys. Chem. B* 108 (2004) 1888.
- [11] C. Hierold, *Advanced Micro & Nanosystems* 8 (2008) 3.
- [12] T. Belin, F. Epron, *Mater. Sci. and Engineering B* 119 (2005) 105.
- [13] T. W. Ebson, P. M. Ajayan, *Nature* 358 (1992) 220.
- [14] P. C. Eklund, B. K. Pradhan, U. J. Kim, Q. Xiong, et al. *Nano Lett.* 2 (2002) 561.
- [15] W. K. Maser, E. Munoz, J. L. Sauvajor, et al. *Chem. Phys. Lett.* 292 (1998) 587.
- [16] M. Kumar, Y. Ando, *J. Nanosci. Nanotechnol.* 10 (2010) 3739.
- [17] R. T. K. Baker, M. A. Barber, P. S. Harris, F. S. Feates, R. J. Waite. *J. Catalysis* 26 (1972) 51.
- [18] R. T. K. Baker, R. J. Waite. *J. Catalysis* 37 (1975) 101.
- [19] J.P. Salvetat, J.M. Bonard, N. H. Thomson, A. J. Kulik, L. Forró, W. Benoit, L. Zuppiroli, *Appl. Phys. A*, 69 (1999) 255.
- [20] B. I. Yakobson, Ph. Avouris, *Topics in Applied Physics*, 80 (2001) 287.
- [21] C. D. Spataru, S. I. Beigi, L. X. Benedict, S. G. Louie, *Phys. Rev. Lett.* 92 (2004) 077 402.
- [22] T. W. Odom, J. L. Huang, P. Kim, C. M. Lieber, *Nature* 391 (1998), 62.
- [23] M. Ouyang, J. L. Huang, C. L. Cheung, C. M. Lieber, *Science* 292 (2001), 702.
- [24] Hong, Seunghun, S. Myung, *Nature Nanotechnology* 24 (2007), 207.
- [25] J. Hone, M. C. Llaguno, N. M. Nemes, A. T. Johnson, J. E. Fischer, D. E. Walters, M. J.

- Casavant, J. Schmidt, R. E. Smalley, *Appl. Phys. Lett.* 78 (2001) 666.
- [26] M. S. Dresselhaus, G. Dresselhaus, J. C. Charlier, E. Hernandez, *Phil. Trans. R. Soc. Lond. A* 362 (2004) 2065.
- [27] G. D. Zhan, J. D. Kuntz, J. Wan, A. K. Mukherjee, *Nature Mater.* 2 (2003) 38.
- [28] A. Phaedon, A. Joerg, M. Richard, *Proceedings of the IEEE*. 91 (2003) 1772.
- [29] S. N. Kim, J. F. Rusling, F. Papadimitrakopoulos, *Adv. Mater.* 19 (2007) 3214.
- [30] K. Sumathy, K. H. Yeung, L. Yong, *Prog Energy Comb Sci.* 29 (2003) 301.
- [31] R. Z. Wang, R. G. Oliveira, *Prog Energy Comb Sci.* 32 (2006) 424.
- [32] F. Meunier, *Appl. Therm. Eng.* 18 (1998) 715.
- [33] R. Soka (Chief Technology Officer, FireChill): Absorption Cooling and Ammonia. 2010
- [34] S. Vasta, G. Maggio, G. Santori, A. Freni, F. Polonara, G. Restuccia, *Energy Conversion and Management*. 49 (2008) 3025.
- [35] G. Cacciola, G. Restuccia. *Int J Refrigerat.* 18 (1995) 100.
- [36] Yu.I. Aristov, M.M. Tokarev, V.E. Sharonov. *Chem. Eng. Sci.* 63 (2008) 2907.
- [37] J.V. Veselovskaya, M.M. Tokarev, Yu. I. Aristov. *Appl. Therm. Eng.* 30 (2010) 584.
- [38] V.E. Sharonov, Yu.I. Aristov. *Chem. Eng. J.* 136 (2008) 419.
- [39] L. Yong, R. Z. Wang. *Recent Pat. on Eng.* 1 (2007) 1.
- [40] Monma, T., Mizota, T. *JP2005299974* (2005).
- [41] Patzner, N. *EP1154208* (2001).
- [42] M. Li , C.J. Sun, R.Z.Wang, W.D.Cai. *Appl. Therm. Eng.* 24 (2004) 865.
- [43] D. Wang, S. Jin, Y. Wu, C. M. Lieber. *Nano Lett.* 3 (2003) 1255.
- [44] P. Jin, Q. Chen, L. Hao, L. Zhang, L. Wang. *J. Phys. Chem. B* 108 (2004) 6311
- [45] X. T. Zhang, O. Sato, M. Taguchi, Y. Einaga, T. Murakami, A. Fujishima *Chem. Mater.* 1(2005) 696.
- [46] H. G. Yang, H. C. Zeng, *J. Phys. Chem. B* 108 (2004) 3492.
- [47] G. Liu, L. Wang, H. G. Yang, G. Q. Lu. *J. Mater. Chem.* 20 (2010) 831.
- [48] J. G. Li, T. Ishigaki. *Acta Mater.* 52 (2004) 5143.
- [49] B. X. Wang, X. P. Zhao. *Adv. Funct. Mater.* 15 (2005) 1815.
- [50] G. M. Whitesides, B. Grzybowski. *Science* 295 (2002) 2418.
- [51] T. K. Sau, A. L. Rogach. *Adv. Mater* 22 (2010) 1781.

- [52] S. C. Roy, O. K. Varghese, M. Paulose, C. A. Grimes, *ACS Nano* 4 (2010) 637.
- [53] A. L. Linsebigler, G. Lu, J. T. Yates. *Chem. Rev.* 95 (1995) 735.
- [54] Z. F. Bian, J. Zhu, F. L. Cao, Y. N. Huo, H. X. Li. *Chem. Commun.* 46 (2010) 8451.
- [55] M. T. Vander, A. Mattson, L. Oesterlund. *J. Catal.* 25 (2007) 131.
- [56] T. Hongo, A. Yamazaki. *J. Mater. Sci.* 45 (2010) 275.
- [57] L. Liu, J. S. Qian, Y. M. Cui, X. F. Zhou, X. F. Guo, W. P. Ding. *Chem. Commun.* 46 (2010) 2402.
- [58] H. Li, Z. Bian, J. Zhu, Y. Huo, Y. Lu. *J. Am. Chem. Soc.* 129 (2007) 8406.
- [59] V. Barone, O. Hod, G. E. Scuseria, *Nano Lett.* 6 (2006) 2748.
- [60] S. Park, R. S. Ruoff, *Nat. Nanotechnol.* 4 (2009) 217.
- [61] C. Niyogi, E. Bekyarova, M. E. Itkis, R. C. Haddon. *J. Am. Chem. Soc.* 128 (2006) 7720.
- [62] A. K. Geim, K. S. Novoselov. *Nat. Mater.* 6 (2007) 183.
- [63] K. Zhou, Y. Zhu, X. L. Yang, X. Jiang, C. Z. Li. *New J. Chem.* 35 (2011) 353.
- [64] V. Subramanian, E. E. Wolf, P. V. Kamat. *Langmuir* 10 (2003) 469.
- [65] K. H. Li, D. M. Jang, T. J. Cho, Y. Kim, J. Park. *J. Phys. Chem. C* 113 (2009) 19966.
- [66] H. Zhang, X. Lv, Y. Li, Y. Wang. *ACS Nano* 4 (2009) 380.
- [67] Q. Liu, Z. Liu, X. Zhang, L. Yang, N. Zhang, Y. Chen, J. Wei. *Adv. Funct. Mater.* 16 (2006) 1975.
- [68] Y. Ou, J. D. Lin, D. M. Liao. *Chem. Phys. Lett.* 429 (2006) 199.

Chapter Two

2.1 Synthesis of CNTs on Metallic Substrate by CVD

As mentioned before, CNTs are one of the most promising materials in many applications due to its outstanding mechanical, electrical and thermal properties. Our aim is to directly synthesize high quality CNTs on metallic substrate, and investigate the interaction between CNTs and refrigerant gas (NH_3) for adsorptive cooling application. Although CNTs are believed to have excellent thermal conductivity, and the theoretical predictions suggest the value as high as $3000\text{--}6600\text{Wm}^{-1}\text{K}^{-1}$ [1, 2], the actual value is always drastically reduced due to the boundary phonon scattering between individual tubes. In this case, a conducting substrate is often required to enhance the thermal/electron transfer. Stainless steel (SS) is an attractive candidate due to its high Fe content ($>66\%$) and feasibility of tailoring to produce active sites for CNTs growth [3]. The synthesis of CNTs on bulk metallic surfaces has been reported by many research groups [4-8]. Most of the research resulted in MWCNTs, while SWCNTs were also observed, but not too many. The reason still remains unclear. Here we present a facile chemical vapor deposition (CVD) approach to grow CNTs on SS wool starting from acetylene. A systematic screening of the growth parameters and growing mechanism will be illustrated in the following sections.

2.1.1 Materials and Instruments

Hydrochloric acid (HCl , 36.5%~38%, reagent grade), acetone (Fisher), acetylene (atomic absorption grade, Airgas), air (high purity, Airgas), hydrogen (ultra high purity, Airgas), argon (high purity, Airgas), stainless steel wool (Type 316L, Palmer)

2.1.2 Experimental

Type 316L grade commercial stainless steel wool (the composition is listed in

Table 2.1) was used as both catalyst and substrate for CNTs growth. A bundle of steel wool (~2.5cm long, 0.5g) were cleaned by sonication in acetone and isopropyl alcohol for 10~15mins each. Prior to use, the SS wool was also etched in HCl (~38%) for 10min.

The CVD furnace used is a Linderg/Blue 5000 series. A quartz tube is located inside the furnace such that most of the tube is covered. The etched SS wool was nicely packed and loaded into the quartz tube sitting in the middle of the furnace temperature zone, parallel to the gas flow. One end of the tube is connected with the inlet of gas flow. The other end is the gas outlet. Gas flow rates are controlled by mass flow meters.

Before CNT synthesis, the SS wool experiences a redox pretreatment (oxidation and reduction) by flowing air and hydrogen, respectively. CNT deposition was carried out at desired temperature for a certain time, then the CNT coated SS wool was annealed at the deposition temperature for another preset time and cooled down to room temperature. The CVD setup is illustrated in Fig.2.1

Table 2.1 Chemical Composition of Austenitic Stainless Steel (Type 316L)

grade (wt.%)	C	Mn	Si	Cr	Ni	Mo	P	S	N	Fe
316L	0.030	2.00	0.75	16-18	10-14	2-3	0.045	0.030	0.01	Bal.

A series of growth parameters were studied to investigate the mechanism and screen out optimum conditions to obtain CNTs with high quality based on our available system, including substrate pretreatment, deposition temperature (T_d), flow rate of gases, carbon source concentration and reaction time, etc.

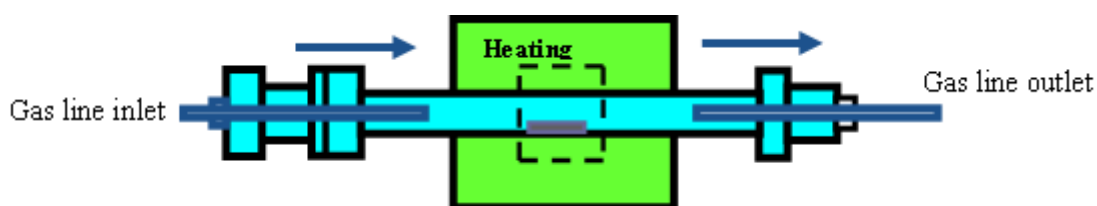


Fig.2.1 Schematic illustration for CVD growth of CNTs

2.1.3 Results and Discussion

A typical photo of SS wool supported CNT sample is shown in Fig.2.2. One of the most important factors which determined CNT quality is the deposition



temperature. We have carried out the investigation on the influence of deposition temperatures to the CNT quality and yield. Detailed growth parameters are summarized in Table 2.2.

Fig.2.2 SS wool before and after CNT deposition

Table 2.2 CNT synthesis with different deposition temperatures

Sample #			1	2	3	4	5	6	7
Substrate Treatment	1. 38.5% HCl etching	No etching							
	2. Air-Oxidation	Ar(ml/min)	300	300	300	300	300	300	300
		Ar(ml/min)	300	300	300	300	300	300	300
		T (°C)	500	500	500	500	500	500	500
		Time(min)	5	5	5	5	5	5	5
	3. H2-Reduction	Ar(ml/min)	300	300	300	300	300	300	300
		H2(ml/min)	300	300	300	300	300	300	300
		T (°C)	500	500	500	500	500	500	500
		Time(min)	5	5	5	5	5	5	5
	CNT synthesis	4. Reaction	Ar(ml/min)	212	212	212	212	212	212
C2H2(ml/min)			309	309	309	309	309	309	309
T (°C)			500	550	600	650	700	750	800
Time(min)			10	10	10	10	10	10	10

Fig.2.3 (a)-(f) illustrates scanning electron microscope (SEM) of CNTs grown on SS wool at 500, 600, 650, 600, 750 and 800°C, respectively. The synthesized CNTs have thick amorphous-like carbon overcoat, which made them look like worms. The average diameters can vary between 25-125nm. At high temperature, the metal atoms agglomerate into bigger clusters, which dominate the diameter of CNTs. The length of CNTs was rather long so that it was difficult to accurately measure them. However, it was obviously longer than 1 μ m. Meanwhile, high temperature promotes more carbon deposition and hence more wall formation [9].

Fig.2.4 shows the relative weight gain of CNTs with respect to different deposition temperatures. The highest CNT yield occurs between 700~750°C, which is believed to be an optimum range for our system and method. In the following research, we chose 700°C as the deposition temperature.

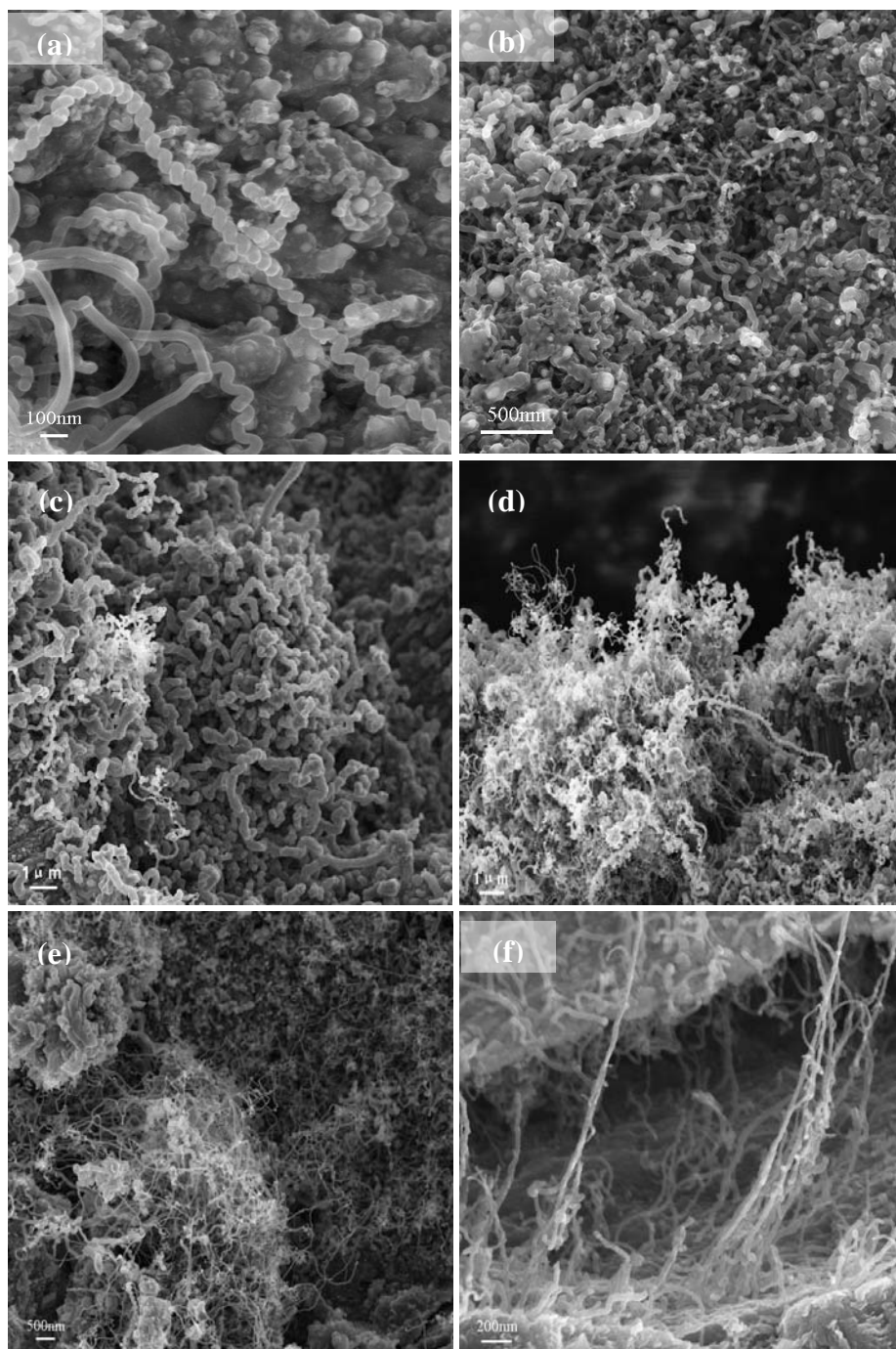


Fig.2.3 CNTs synthesized at various deposition temperatures
(a) 500°C; (b) 600°C; (c) 650°C; (d) 700°C; (e) 750°C; (f) 800°

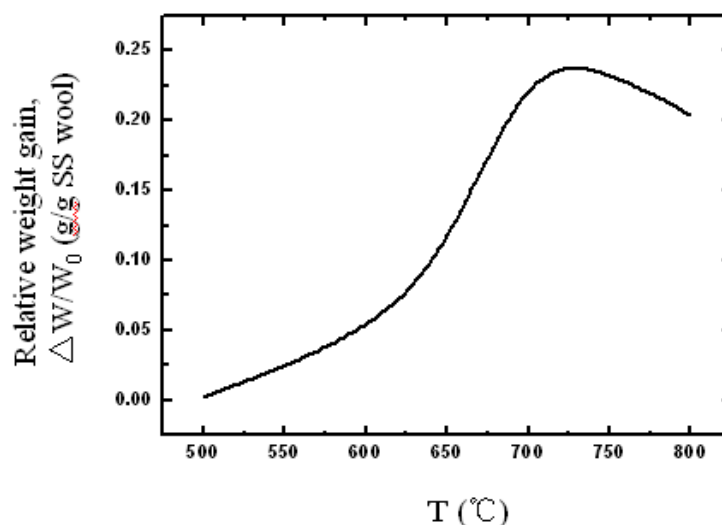


Fig.2.4 Relative weight gain of CNTs with respect to deposition temperature

The CNTs growth rate was quite low at relatively lower temperatures (500°C-600°C). It was noticed that extremely short-length CNTs or CNT seeds emerged at the surface of catalyst particles (Fig.2.5). It suggests that at lower temperatures, due to the strong interaction of Fe-C alloy with the substrate (catalyst feed stock), the CNTs grow via a base-growth process, while a profound growth of CNT was observed at 650°C and higher temperatures. The metal particles were encapsulated at the CNT tips. It suggests that at higher temperatures, tip-growth process takes place, although we still can't exclude the possibility that base-growth process coexists.

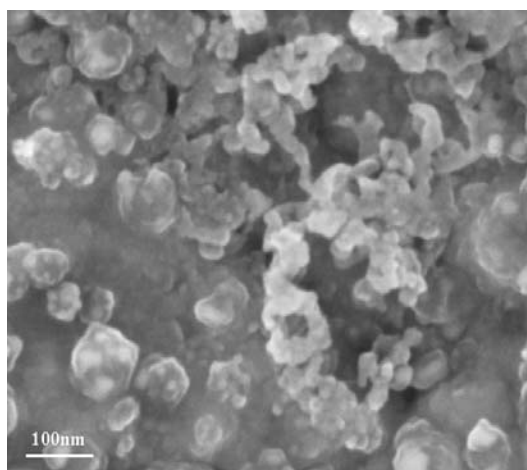


Fig.2.5 SEM micrograph of CNT “seeds” on top of the metallic catalysts

Metallic surface conditioning prior to CVD process was also investigated. Stainless steel substrates here acted as supports for nanotube growth, but they are still lack of free metallic iron particles which can serve as the catalysts for CNT growth [7]. The objective of surface conditioning was to enhance or activate the latent activity of metallic surface by forming granular nanostructures. In addition, the surface becomes more homogenous after pretreatment, which is important for uniform growth of CNTs. It is believed that the growth of CNTs on stainless steel by thermal CVD method was due to the existence of Fe, Ni and probably also Mo elements.

Stainless steel substrate was treated with acid followed by preheating under air and hydrogen. The SS wool samples with different acid treatment times of 1, 5, 10min together with the as-received sample (as the control sample) were studied to elucidate the surface properties on CNT growth. Fig.2.6 shows the SEM images of

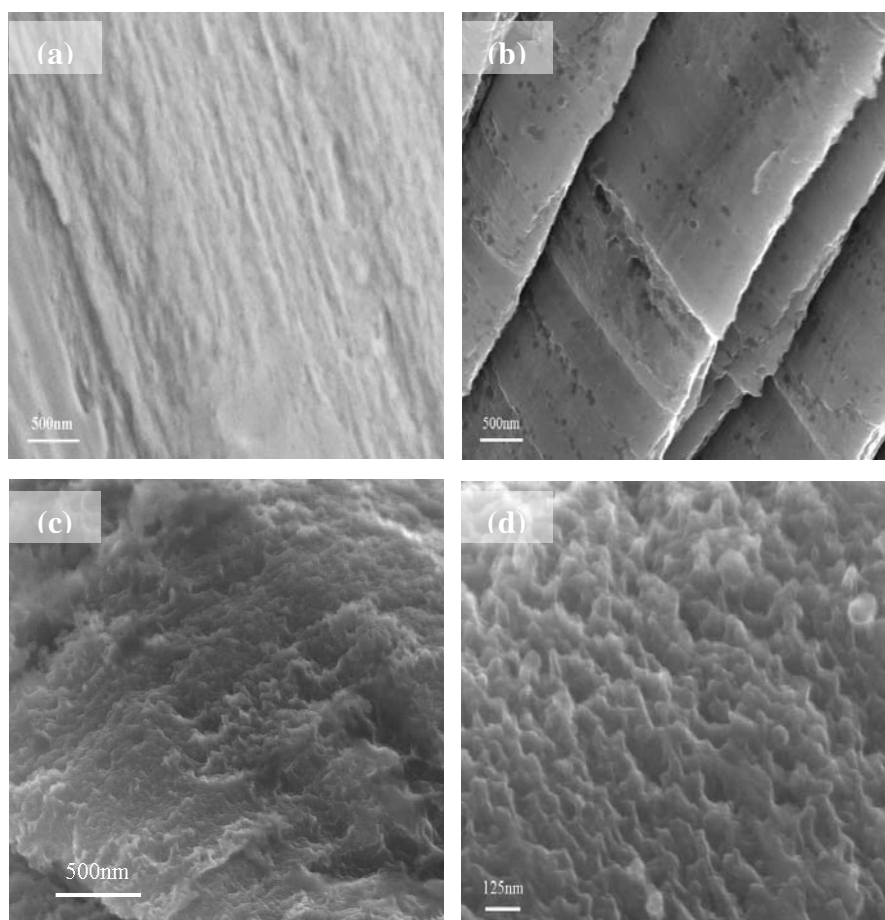


Fig.2.6 SS wool substrate treated with HCl (~38%) for different times

(a) 0min, (b) 1min, (c) 5min, (d) 10min

SS wool treated for different times.

The SS wool as received has a passive layer (mainly composed of Cr_2O_3) which gives initial protection to the stainless steel from corrosion. Chromium layer gradually dissolves in the acid during the etching process. Mesoporous iron oxide film forms on the surface of the substrate, which is favorable for CNT growth. For SS wool treated with 1min, only partial passive layer is etched (see Fig.2.6b). As the etching time increases, the formation of mesoporous iron oxide film becomes complete, which results in a rough surface (as shown Fig.2.6d).

The next step is a redox treatment (air oxidation and hydrogen reduction). During air oxidation, once the steel wool is heated, island-like fine granular structures were formed, which increased the surface area and acted as catalyst sites. The diameter of the formed granular structures highly depended on the treatment temperatures [10], which increased the surface area and acted as catalyst sites. Fe and Ni would react with C from C_2H_2 to form carbon-metal alloy particles and induced CNTs growth. Since the catalytic elements Fe and Ni would be deactivated due to oxidation, reactivation of these catalyst particles by a further reduction by H_2 was necessary for keeping their catalytic activity. Details of this oxidation-reduction pretreatment prior to CVD process has also been thoroughly discussed by Wal RLV [5]. It's also believed that oxygen oxidation would decrease the necessary time of preheating.

Fig.2.7 (a)-(f) illustrates the SEM images of the formed CNTs after the SS wool pretreated at different temperatures. When the SS wool was treated at 500°C for 1h, CNTs were formed and interspersed with significant amounts of amorphous carbon. The average diameter of CNTs varied from 50-80nm (sometimes with a few in the range of 80-110nm). It also can be observed that diamond-like structures were formed, as shown in Fig.2.8. When the preheating temperature increased, the amount of amorphous carbon was reduced while the density of CNTs increased. This is apparently observed when the steel wool was preheated at 700°C and 750°C (see Fig.2.7e,f).

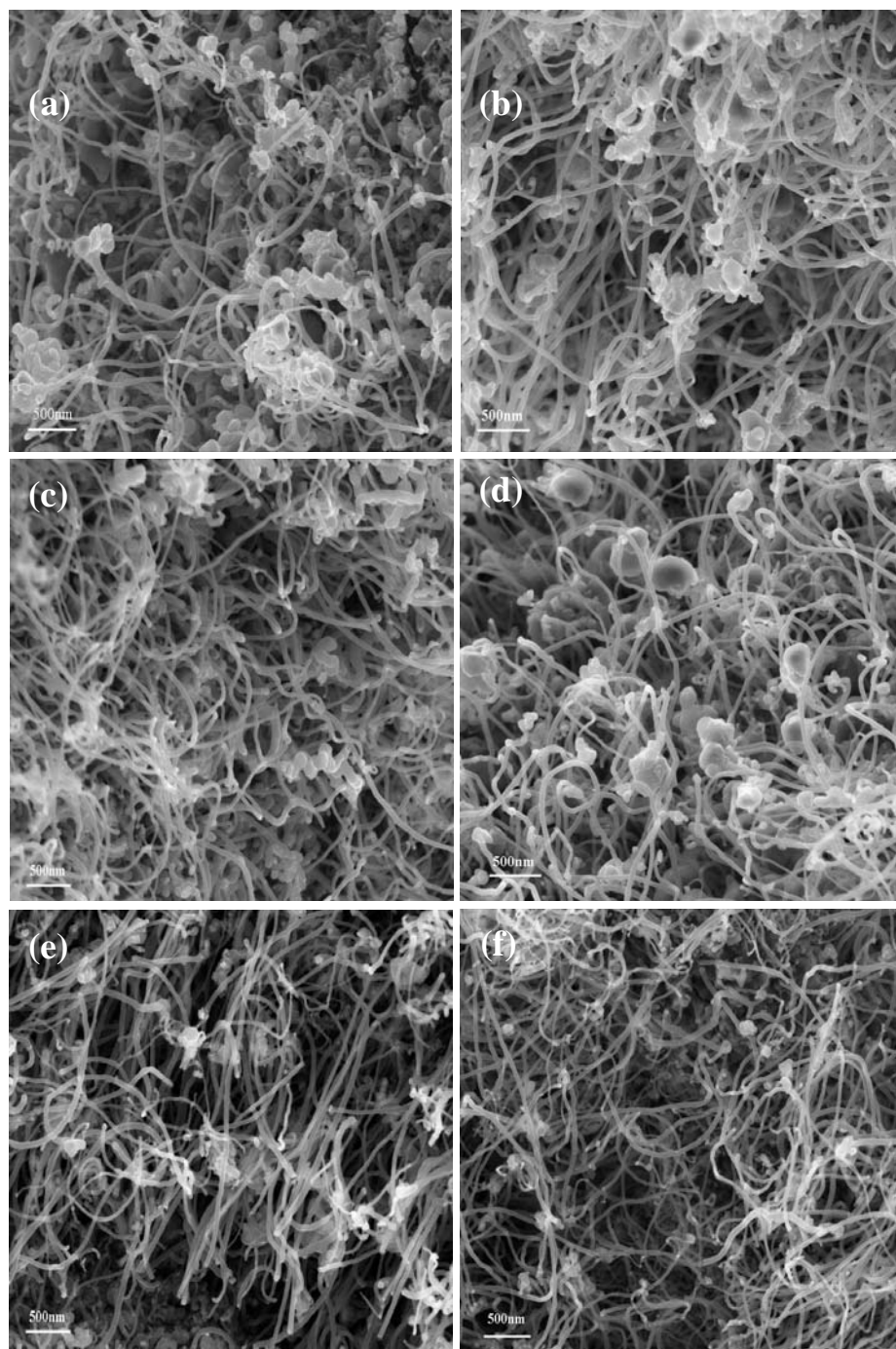


Fig.2.7 SEM images of CNTs grown on SS316L with different preheating temperatures:
(a) 500 °C; (b) 550°C; (c) 600°C; (d) 650°C; (e) 700°C; (f) 750°C

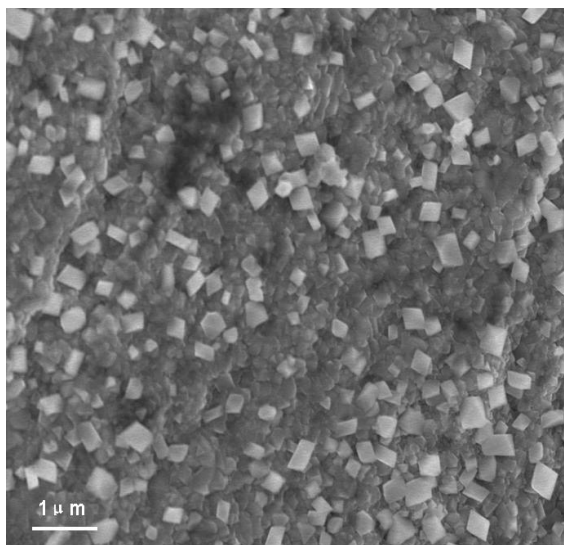


Fig.2.8 SS wool conditioned at 700°C (HCl treated).

Island-like structures with diamond-like particles were formed

Besides deposition temperature and substrate pretreatment, the gas flow rates are also influential to CNT growth. The flow rate affected the residence time (the time that a gas molecule spent in the tube) and the number of active molecules available for decomposition per unit time. Lower flow rate decreased the number of gas molecules undergoing decomposition/unit time, while increasing the residence time:

$$\tau = \frac{\pi \cdot d^2}{4 \cdot L \cdot F}$$

τ - the residence time; d -diameter of the glass tube; L -length of the tube before the steel wool; F -flow rate of the gas. At higher flow rates, the number of available gas molecules increases, resulting in more molecules decomposed at a given time. Higher flow rates also facilitate molecules to travel further along the tube before deposition. This is supposed to result in increased carbon species coverage on steel wool in the direction of gas flow. After CVD process, post-annealing treatment is helpful to burn off non-tubular carbonaceous species, which mainly consisted of amorphous carbon.

Combining the parameters we investigated, we successfully obtained vertically

aligned CNTs (VACNTs) with high yield and quality, which are shown in Fig.2.9. Few amorphous carbon were observed and the diameter of CNTs is dramatically reduced to 20~30nm (see Fig.2.9b inset).

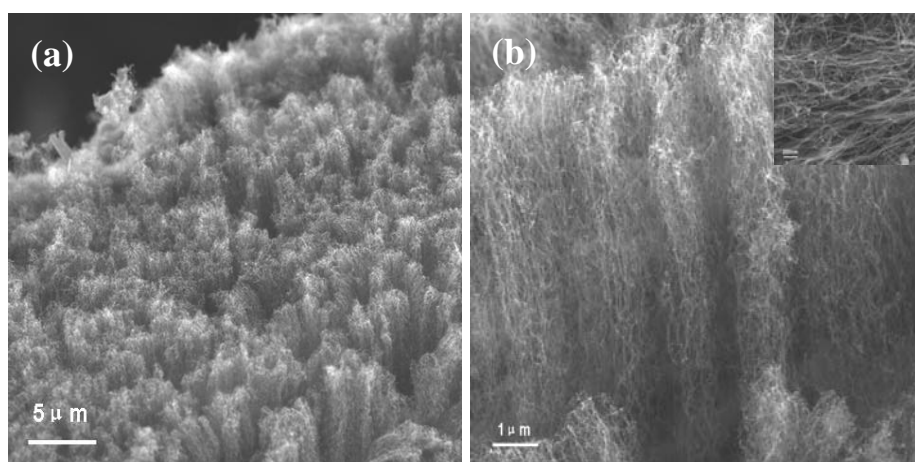


Fig.2.9 Vertically aligned CNT forest at optimized condition.

(a) Top view of the forest, (b) 30° tilt image of vertically aligned CNTs (The inset images shows the cross-linking of CNTs with diameter about 20~30nm)

The protocol described here can be improved based on needs by the further understanding of the CNT growth mechanism on conducting substrates. It has been demonstrated that the quality and intrinsic properties of CNTs can be further improved by including some gaseous additive (e.g. H_2/H_2O) or abrupt termination techniques are applied [11, 12]. These will also be systematically studied in our further research.

In conclusion, an efficient and cost-effective way to synthesize highly aligned CNTs on stainless steel substrate without any external catalysts was presented. The method is easy to scale up and can be applied to larger SS surfaces and other geometries for industrial applications. It has been hypothesized that the utilization of the in-situ formed catalysts on a metallic substrate could enhance the adherence and electronic/thermal contact of CNTs to the metallic substrates. Considering the highly hierarchical porous structures of the SS wool (important for mass transport for refrigerant gases), it is reasonable to expect that a better cooling efficiency can

be achieved when the produced SS wool/CNT hybrid materials are used as the absorbents, which will be studied in the near future.

2.2 Adsorptive heat transformation study for solid adsorbents

In this part of work, we use ammonia as our refrigerant gas to study the heat transformation property for different adsorbents. Although ammonia received impingement due to its toxicity, unpleasant smell and difficulty in handling over the past several years, we can't underestimate ammonia as an outstanding candidate for refrigerant choice because of its commercial, operational, energy and environmental benefits [13]. Ammonia has zero ozone depletion potential and no contribution to greenhouse effect responsible for global warming. In addition, it has favorable thermodynamic properties which require less energy to produce refrigeration than many other refrigerants.

Here we use our home-built system to investigate the sorption characteristics of NH_3 /solid adsorbents as working pairs. To check the validity of our system, we first studied the thermodynamic behavior of traditional $\text{BaCl}_2\text{-NH}_3$ working pair in a vermiculite matrix and thermodynamic performance evaluation for other promising adsorbents, including commercialized MWCNTs, SWCNTs. In future studies, we will use our SS wool supported CNTs to investigate the SS wool based CNT- NH_3 interaction and resultant adsorptive cooling effect.

2.2.1 Materials and Instruments

NH_3 , BaCl_2 , Vermiculite, SWCNTs, MWCNTs, SS wool supported CNTs
Home-made setup for isosteric measurement (specific description provided in the following Experimental part)

2.2.2 Experimental

a. Apparatus

The experimental apparatus consists of LoggerPro 3.2, adsorbent chamber, gas

buffer tank, heating tape/oven, connecting pipe, pressure gauge, thermocouple, valves and a vacuum line. A schematic drawing of the experimental setup is shown in Fig.2.10 and a corresponding photograph is shown in Fig.2.11. The adsorbent samples are loaded into the chamber (1). The chamber is within a thermostatic oven or covered by heating tapes in order to maintain the temperature of vessel with adsorbents. A thermocouple is placed near the wall of adsorbent chamber and connected to LoggerPro device to monitor the adsorbent temperature. A pressure gauge was also connected to monitor the pressure change of the system during NH_3 absorption and desorption.

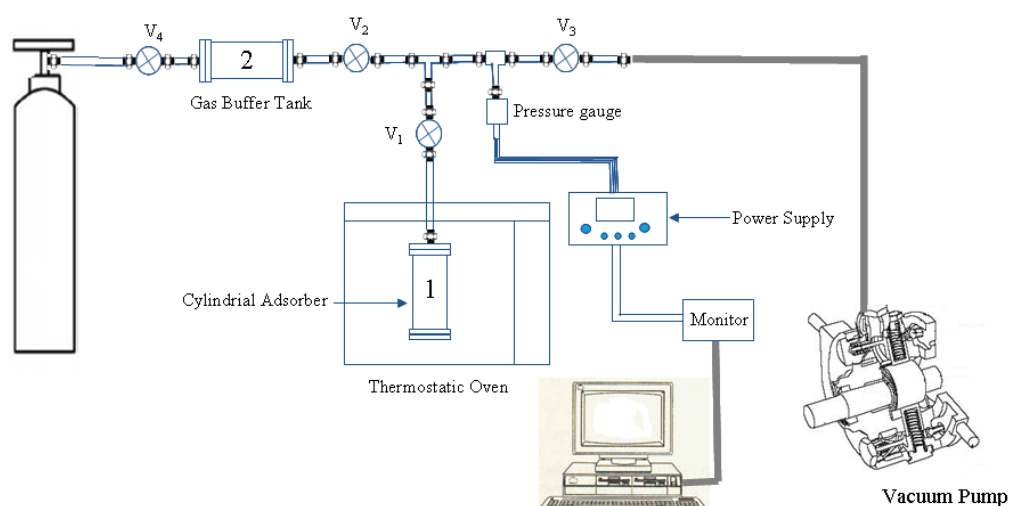


Fig.2.10 Scheme of experimental setup for NH_3 sorption isosteres measurement

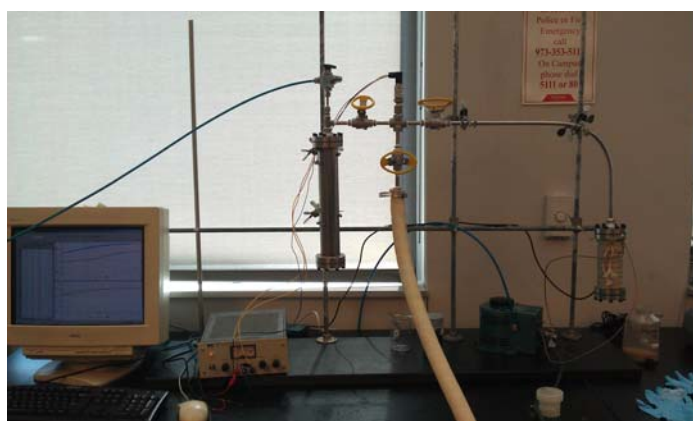


Fig.2.11 A photograph of realistic setup in the lab

b. Adsorbent sample preparation

Three samples were studied: BaCl_2 /vermiculite composite, SWCNTs and MWCNTs purchased from China. BaCl_2 /vermiculite was prepared by immersing the host matrix vermiculite into 25wt.% BaCl_2 aqueous solution, followed by drying in air at 70°C . The other samples were used as received. Before the experiments, all samples were heated to 180°C and cooled to room temperature in dry air. Then initial mass m_0 was measured.

c. Isosteric(IS) measurement

The sample was loaded into the chamber and evacuated for 20-30min (V_1 - V_3 were open and V_4 closed). Then the following procedure was employed for IS measurement.

- (1) The buffer tank was pressurized to initial pressure P_0 (V_2 , V_4 open, V_1 , V_3 closed)
- (2) NH_3 adsorption was started and continued for at least 2h until it reached equilibrium (V_1 , V_2 open, V_3 , V_4 closed).
- (3) Adsorption was terminated when the pressure decreased to P_1 (V_2 open, V_1 , V_3 , V_4 closed).
- (4) Equilibrium pressure P_{eq} was recorded after sorption was finished (V_1 open, V_2 - V_4 closed)

P_{eq} was recorded at room temperature first, and the adsorbent temperature was increased step by step and a whole set of P_{eq} was recorded. P_{eq} change was recorded during the temperature decreases. We obtained isosteric measurement of ammonia sorption by plotting $\ln P_{\text{eq}}$ vs. $1/T$ (K).

2.2.3 Results and Discussion

a. BaCl_2 - NH_3 working pair in vermiculite matrix

A typical sorption cycle for BaCl_2 - NH_3 at pseudo-equilibrium is represented in Fig.2.12. First we saturated the adsorbents with ammonia and waited until it was at equilibrium. Then the temperature was increased stepwise to desorb

ammonia from $\text{BaCl}_2/\text{vermiculite}$. It can be seen that the desorption curve is composed of three basic processes. The first process is thermal expansion (ε), during which no significant desorption occurs. When the temperature reached the minimum temperature required for desorption, pressure increased much faster. When desorption completed, the larger slope compared with the one before desorption indicated more free gas molecules in the system. Then the temperature was decreased stepwise in reverse to examine the adsorption-desorption reversibility. As we can see from Fig.2.12, a large hysteresis loop was observed and the adsorption occurs around 35°C .

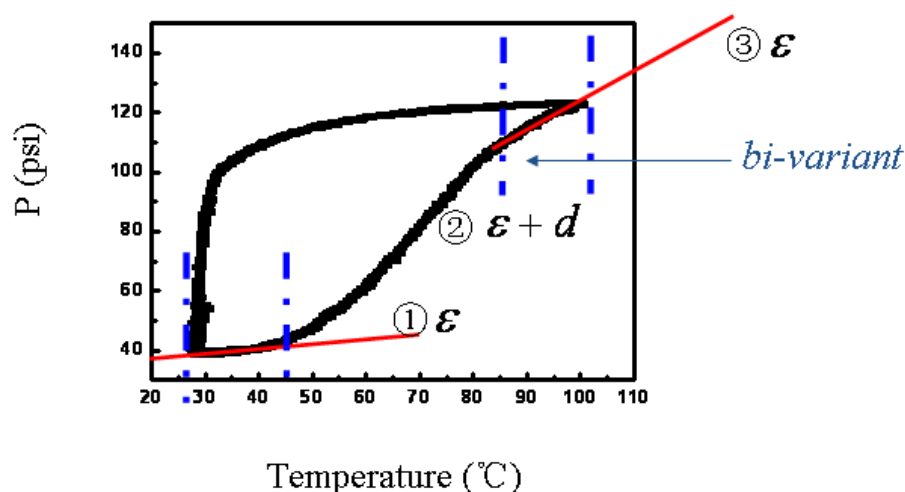
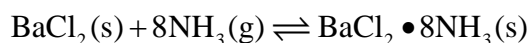


Fig.2.12 A typical adsorption-desorption cycle for $\text{BaCl}_2\text{-NH}_3$ working pair. (The P-T desorption curve consists of thermal expansion and desorption, which results in the difference of slopes. The adsorption occurs at about 35°C . A huge hysteresis loop is also observed, which demonstrated a bi-variant behavior.)

According to Gibbs phase rule, the degree of freedom ν is related to the number of components (k), phases in thermodynamic equilibrium (f) and independent reactions (r). It can be calculated as [14, 15]

$$\nu = k - f - r + 2$$

Regarding to the reaction which took place in this system,



we have three components, three chemical phases (BaCl_2 (s), NH_3 (g) and $\text{BaCl}_2 \cdot 8\text{NH}_3$ (s)) and one independent reaction. Hence, the system is supposed to be mono-variant.

$$\nu = 3 - 3 - 1 + 2 = 1$$

However, it was observed that the P-T diagram showed us a bi-variant behavior due to the existence of hysteresis loop. Similar results were also reported for hydration of $\text{Ca}(\text{NO}_3)_2$ in silica gels [16]. One possible reason for this discrepancy from Gibbs phase rule is the formation of non-uniform crystals, which may have their own synthesis-decomposition behavior, such as the temperature and pressure [15]. In addition, during the synthesis and decomposition of composites, the crystal lattices have been expanded or contracted. The hysteresis may be also caused by the activation barrier for the energy required to expand the crystals, which is irreversible energy loss during one adsorption-desorption cycle [17, 18]. Another possible explanation is the temperature difference between gas temperature (T_g) and temperature within solid particles (T_s). Specifically, $T_g > T_s$ during decomposition and $T_g < T_s$ during synthesis. The temperature lag is caused by exothermic synthesis and endothermic decomposition.

The isosters of ammonia sorption were plotted by $\ln P$ vs. $1/T$ (K) using a linear fitting (see Fig.2.13). The relationship between pressure P and temperature T at equilibrium was determined by the Van't Hoff equation:

$$\ln P = -\frac{\Delta H_m}{RT} + \frac{\Delta S_m}{R}$$

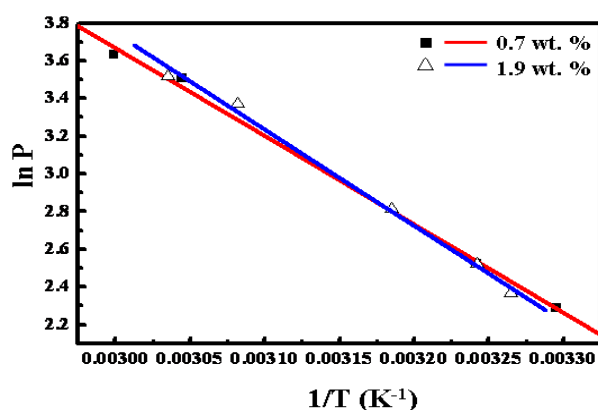


Fig.2.13 Isosters of ammonia sorption on BaCl_2 /vermiculite composite

■ -0.7 wt.%, △ -1.9 wt.%

ΔH_m and ΔS_m are standard

enthalpy and entropy for the reaction. The isosteres are plotted for both desorption and adsorption to get the average value with different NH_3 uptake (0.7 wt.% and 1.9 wt.%). The NH_3 uptake by the adsorbents can be calculated by

$$w_1 = \left[\frac{(P_0 - P_1)V}{RT} - \frac{P_{\text{eq}} V_1}{RT} \right] \frac{\mu}{m_0}$$

where P_0 is initial NH_3 pressure, P_1 is preliminary estimated pressure and P_{eq} is NH_3 pressure at equilibrium. In this equation, V is volume restricted by valve V_1 , V_3 and V_4 in Fig.2.10, volume V_1 is restricted by V_2 and V_3 [19]. The enthalpy and entropy measured were compared with literature values. The calculated standard enthalpy and entropy were -36.5 kJ/mol and -142.5 J/(mol K) for 0.7 wt. % and -38.3 kJ/mol, -149.4 J/(mol K) for 1.9 wt. %, respectively ($\Delta H_m = -36.7$ KJ/mol, $\Delta S_m = -131.8$ J/(mol K) in literature [19]).

It can be seen that the enthalpy was similar to literature value while the absolute value of entropy is a little higher than reported. From the thermodynamic properties, their adsorptive cooling performance can be estimated by using the measured isosteric chart.

b. MWCNTs and SWCNTs

NH_3 adsorption-desorption behavior on commercial MWCNTs and SWCNTs was also studied in a similar way described in experimental part, the isoster measurements are shown in Fig.2.14. The calculated enthalpy and entropy of SWCNTs, MWCNTs and BaCl_2 /vermiculite are shown in Table 2.3. Compared with BaCl_2 /vermiculite, the “van-Hoff” enthalpy and entropy of CNTs are significantly smaller than what we were expecting. One possible explanation is that the interaction between CNTs and NH_3 is physi- sorption and they did not form complexes such as $\text{BaCl}_2\text{-NH}_3$. Instead, when the sample is saturated with NH_3 and reached its adsorption equilibrium, and we increased the temperature to desorb all the ammonia adsorbed on CNTs, the difference of the number of NH_3 gas molecules before and after desorption was calculated to evaluate the NH_3

adsorption capacity, which are shown in Table 2.4.

$$n = \left(\frac{P_e}{T_e} - \frac{P_i}{T_i} \right) \cdot \frac{V}{R \cdot m} \text{ (mol / g)}$$

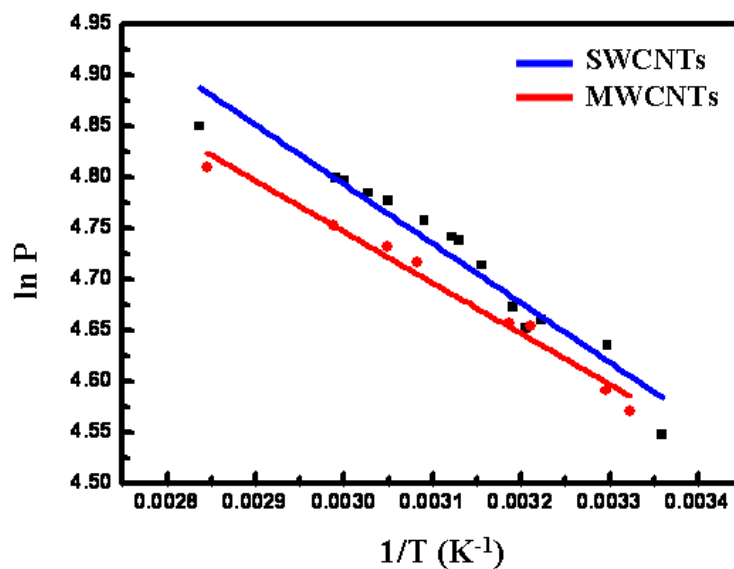


Fig.2.14 Isosters of ammonia sorption on SWCNTs and MWCNTs

Table 2.3 Enthalpy and entropy of ammonia sorption on
BaCl₂/vermiculite, SWCNTs and MWCNTs

Ammonia uptake		ΔH (KJ/mol)	ΔS (J/mol K)
adsorbents	wt. %		
BaCl ₂	0.7	-36.5	-142.5
BaCl ₂	1.9	-38.3	-149.4
SWCNTs	-	-4.27	-124.1
MWCNTs	-	-6.14	-130.7

Table 2.4 NH₃ adsorption capacity calculation for different adsorbents

P _i (psi)	T _i (°C)	P _e (psi)	T _e (°C)	V(cm ³)	m(g)	n(mol/g)
BaCl₂/Vermiculite						
14.55	25.3	20.43	30.3	335.47	183	2.82E-05
14.55	25.3	41	45.3	335.47	183	0.00012
14.55	25.3	51.27	55.3	335.47	183	0.00016
MWCNTs						
77.411	24.1	80.349	29.3	295.54	4.9885	0.00026
77.411	24.1	96.504	61.2	295.54	4.9885	0.0014
77.411	24.1	109.723	99	295.54	4.9885	0.0017
SWCNTs						
77.411	19.8	82.111	25.6	295.54	7.1733	0.00036
77.411	19.8	103.848	58.4	295.54	7.1733	0.0017
77.411	19.8	112.366	88.7	295.54	7.1733	0.0016

(P_i, T_i are initial pressure and temperature, P_e, T_e are pressure and temperature at equilibrium, V(cm³) is volume which is not occupied by adsorbents, m(g) is mass of adsorbents, n(mol/g) is the maximum number of NH₃ gas molecules desorbed from adsorbents at enough high temperature)

The results demonstrate that NH₃ capacity of CNTs is more than ten times higher than BaCl₂/vermiculite. Fig.2.14 was plotted by the number of NH₃ gas molecules adsorbed on unit mass of adsorbents vs. temperature. It can be observed that the number of NH₃ molecules adsorbed significantly increased at a certain temperature range for both SWCNTs and MWCNTs, in which NH₃ adsorption-desorption occurs. The desorption took place around 33°C~55°C for SWCNTs and 55°C~67°C for MWCNTs, respectively.

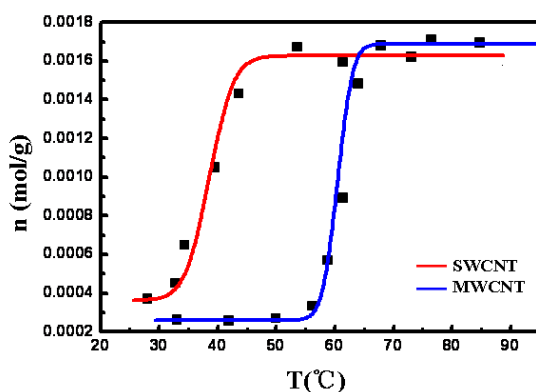


Fig.2.14 NH₃ sorption on SWCNTs and MWCNTs. The height between two plateaus of each curve indicates NH₃ capacity of CNTs, two different ad-desorption temperatures are observed.

Fig.2.15 shows the P-T diagram

for NH_3 adsorption-desorption on SWCNTs and MWCNTs. Compared with $\text{BaCl}_2/\text{vermiculite}$, there has been a significant diminishing hysteresis, indicating a better reversibility of NH_3 sorption behavior. In addition, The NH_3 adsorption-desorption cycle was repeated more than three times. It is observed that when we heat CNTs to desorb NH_3 ($70\sim 90^\circ\text{C}$) and cool down to initial temperature, the pressure decreases to an even lower stage than the last cycle. It has been reported that thermolysis of oxygen containing functionalities on carbon nanotubes can result in permanent entrapment of light gas molecules like CO_2 [20]. The pressure decrease in our study probably can be attributed to the generation of permanently trapped NH_3 gas molecular species within CNTs, although detailed mechanism still needs further investigation.

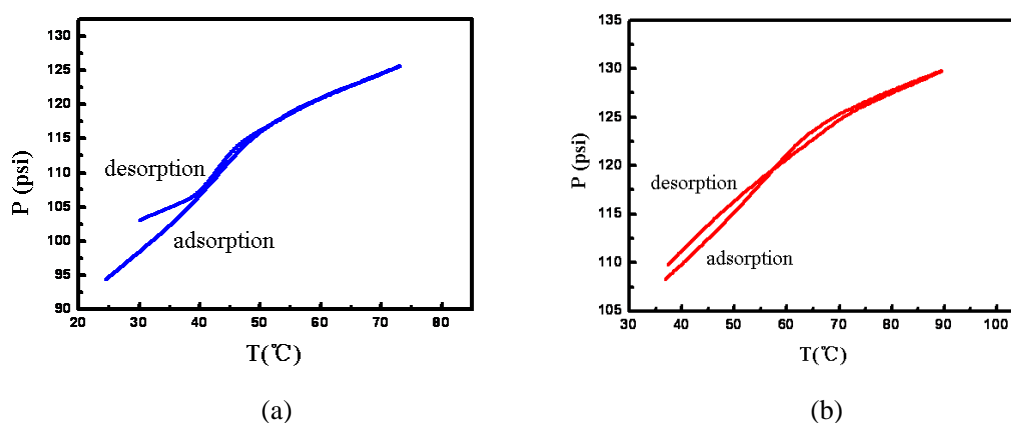


Fig.2.15 P-T diagram of NH_3 adsorption-desorption on
(a) SWCNTs, (b) MWCNTs

In summary, in this part of the work, we successfully synthesized stainless steel wool supported CNTs without any external catalysts by chemical vapor deposition. Different growth parameters such as deposition temperature and substrate pretreatment were studied to improve the quality of CNTs. Vertically aligned CNT forests were obtained and characterized mainly with SEM.

Furthermore, a convenient system was designed for thermodynamic study of NH_3 adsorption on different solid adsorbents ($\text{BaCl}_2/\text{vermiculite}$, SWCNTs, MWCNTs). The adsorption-desorption behavior was analyzed by P-T diagram and

thermodynamic properties such as equilibrium enthalpy and entropy were evaluated. Future work will be focused on the thermodynamic study of our SS wool based CNTs and investigation of adsorptive cooling effect (COP, SCP) of adsorbents of our interests.

References

- [1] J. Che, T. Cagin, W. A. Goddard, *Nanotechnology*, 11 (2000) 65.
- [2] S. Berber, Y. Kwon, D. Tomanek, *Phys. Rev. Lett.* 84 (2000) 4613.
- [3] C. E. Baddour, F. Fadlallah, D. Nasuhoglu, R. Mitra, L. Vandsburger, J. L. Meunier. *Carbon* 47 (2003) 313.
- [4] L. Yuan, K. Saito, W. Hu, Z. Chen. *Chem. Phys. Lett.* 346 (2001) 23.
- [5] R. L. V. Wal, L. J. Hall. *Carbon* 41 (2003) 659.
- [6] C. Pan, Y. Liu, F. Cao, J. Wang, Y. Ren. *Micro.* 35 (2004) 461.
- [7] M. Charan, W. Bing, *Langmuir* 23 (2007) 9046.
- [8] K. Mahesh, I. Zafar, M. Somenath. *Carbon* 44 (2006) 1235.
- [9] M. Kumar, Y. Ando. *J. Nanosci. Nanotechnol.* 10 (2010) 3739.
- [10] W. Z. Li, J. G. Wen, Z. F. Ren. *Appl. Phys. A.* 2002(74) 397.
- [11] B. Kim, H. Chung, K. H. G. Yoon, C. J. Lee, W. Kim. *Synthetic Metals* 160 (2010) 584.
- [12] E. R. Meshot, A. J. Harta. *Appl. Phys. Lett.* 92 (2008) 113107.
- [13] R. Soka (Chief Technology Officer, FireChill): Absorption Cooling and Ammonia. 2010.
- [14] A. Yu, M. A. Boles. Thermodynamics: An Engineering Approach. *McGray-Hill Inc.* 2002.
- [15] Y. Zhong, R. E. Critoph, R. N. Thorpe, Z. T. Telto, Y. I. Aristov. *Appl. Therm. Eng.* 27 (2007) 2455.
- [16] I. A. Simonova, Y. I. Aristov. *Rus. J. Phys. Chem.* 79 (2005) 1307.
- [17] J. Trudel, S. Hosatte, M. Ternan. *Appl. Therm. Eng.* 19 (1999) 495.
- [18] A. Marty. *J. Therm. Anal.* 37 (1991) 479.
- [19] J. V. Veselovskaya, M. M. Tokarev, Yu. I. Aristov. *Appl. Therm. Eng.* 30 (2010) 584.
- [20] C. Matranga, L. Chen, M. Smith, E. Bittner, J. K. Johnson, B. Bockrath. *J. Phys. Chem. B* 107 (2003) 12930.

Chapter Three

3.Synthesis of TiO₂/Graphene Composite Photocatalysts

As a wide band gap semiconductor material, titania (TiO₂) is particularly noteworthy due to its excellent photocatalytic activity and chemical stability. However, its performance is always limited by the relatively fast electron-hole pair recombination and the agglomeration of nanoparticles in reality. With the advance of carbon based materials, graphene is quickly being accepted to be a good support for TiO₂ to enhance the photocatalytic activity due to its unique electronic properties. Graphene-based TiO₂ nanocomposites have been reported in terms of the enhanced photocatalytic activities [1-4].

Herein, we successfully prepared TiO₂ nanorods/graphene composites via hydrothermal reaction using TiCl₃ saturated NaCl solution as raw materials. The products were studied by scanning electron microscopy (SEM), Raman spectroscopy and UV/Vis diffuse reflectance spectroscopy.

3.1 Materials and Instruments

Titanium (III) chloride (TiCl₃, ca. 10wt.% solution in 20~30 wt.% hydrochloric acid, Aldrich), sodium chloride (NaCl, Aldrich), urea (reagent grade, 99.0-100.5%, Aldrich), graphene (synthesized in our lab), DI water. Raman spectrometer, electric oven, Teflon-lined stainless steel autoclave (AC4744, Parr), Scanning electron microscope (SEM, Hitachi S-4800), UV-vis spectrometer (Cary 500)

3.2 Experimental

Preparation

A certain amount of titanium trichloride solution (~10wt.% in 20~30% HCl) was added into freshly saturated NaCl (in water) and urea was added as an additive. Then graphene (dispersed in water) was added dropwise with vigorous stirring and the mixture was sonicated for 40-50min in a sonication bath to make

sure all species are well dispersed. The purple solution was transferred into a 50 mL Teflon-lined stainless steel autoclave and heated at 175°C for desired time. The product was washed with DI water and ethanol several times and centrifuged and dried at 60°C in air. Detailed procedure is illustrated in Fig.3.1.

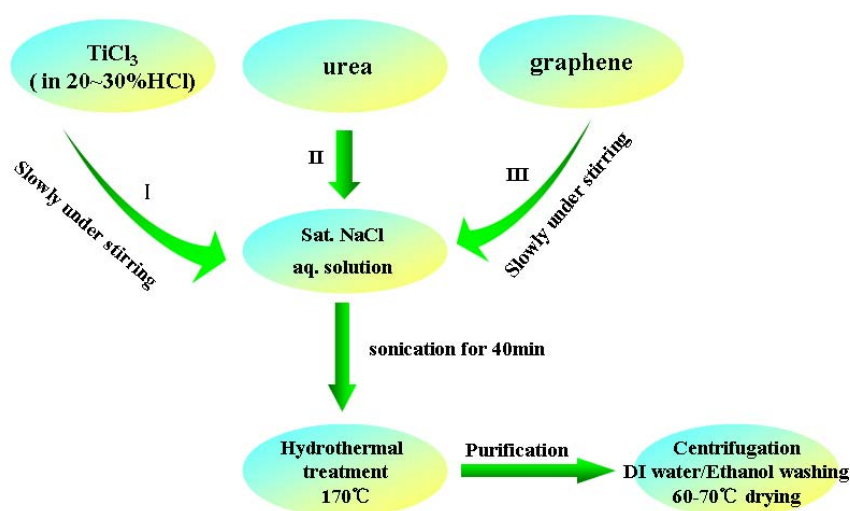


Fig.3.1 Procedure for hydrothermal synthesis of TiO_2 nanorods/graphene composites

Characterization

The morphology and size of products were observed using scanning electron microscope (SEM). The chemical composition was analyzed by Raman spectroscopy. The UV/Vis absorption spectra were recorded with a Cary 500 Scan spectrometer.

3.3 Results and Discussion

3.3.1 Morphology of TiO_2 Nanorods/Graphene Composites

Fig. 3.2(a) shows typical top view SEM images of large scale assembly of microspheres comprised of TiO_2 nanorods, which are prepared with 0.15 M TiCl_3 solution at 175°C for 4h. The hierarchical microspheres have diameters ranging

from 4~6 μm . We are able to see that the nanorods are growing from the core of microspheres (Fig.3.2b). Fig.3.2c-d demonstrate TiO_2 nanorods assembled as arrays on big graphene sheets. Some scattered nanorods were also observed on top of the sheets. Individual TiO_2 nanorods are shown in a flat square-shaped crystallographic planes with diameters about 80 nm in tetragonal cross-section (Fig.3.2e). It's observed that

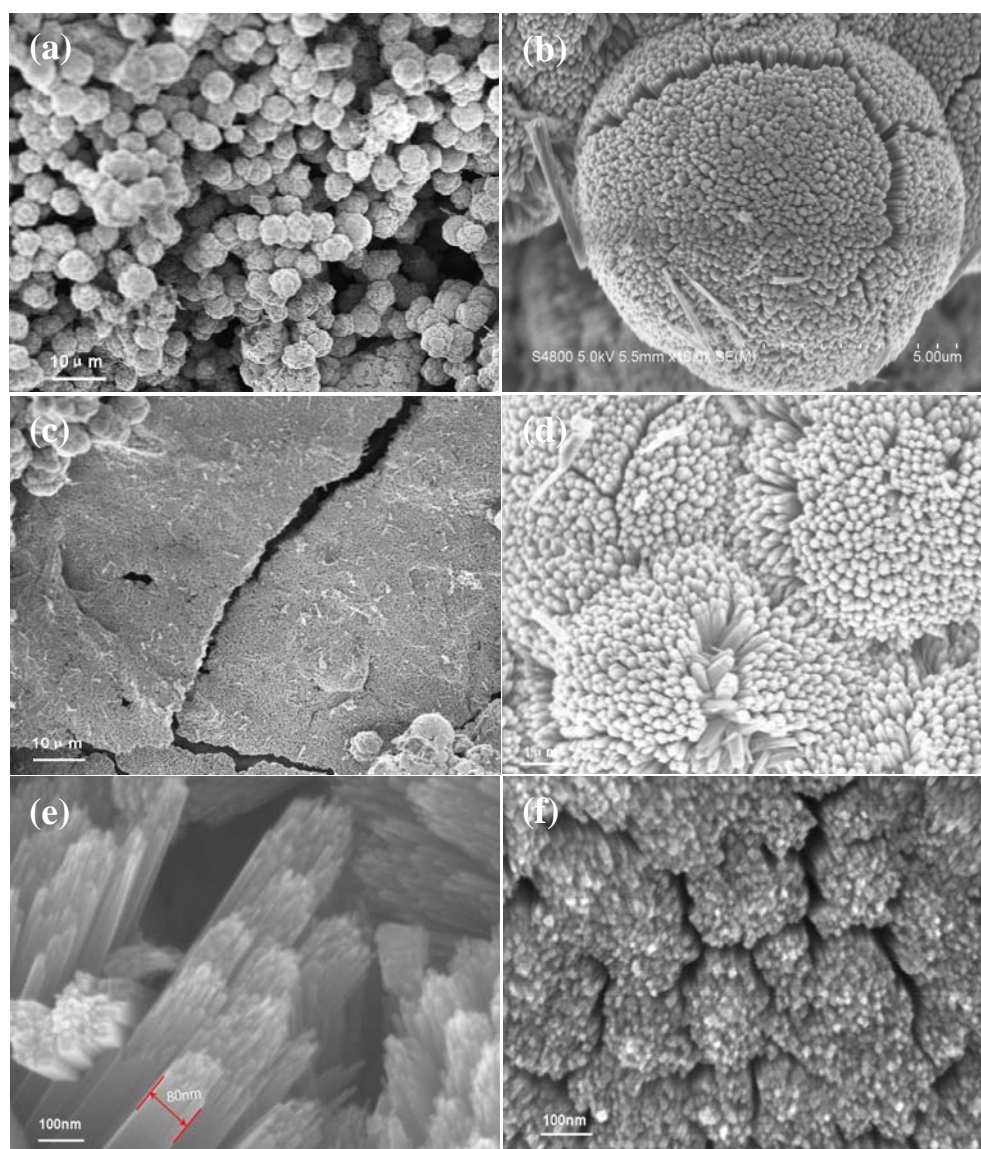


Fig.3.2 SEM images of TiO_2 /graphene composites. (a) large scale of urchin-type TiO_2 microsphere assembly, (b) individual microsphere assembled by TiO_2 nanorods, (c)-(d) nanorod arrays on graphene sheets, (e) cross section view (f) top view of individual TiO_2 nanorods with rough surface comprised of many small particles, indicating a more active growth facet

many small particles exist on the top of nanorods, which indicates a preferential growth along this direction [5]. It is reported that the (001) face is the most active facet for rutile TiO_2 nanorods [6], so this direction is very likely to be [001] direction. This can be confirmed with HRTEM characterization in future study. Fig.3.2f is a top view of TiO_2 nanorods arrays with a rough surface.

In order to understand the formation of urchin type hierarchical TiO_2 /graphene composites, we investigated a time-dependent morphology evolution of the composites. Fig.3.3 shows SEM images of synthesized samples with different reaction times. As shown in Fig.3.3a, the composites obtained after hydrothermal

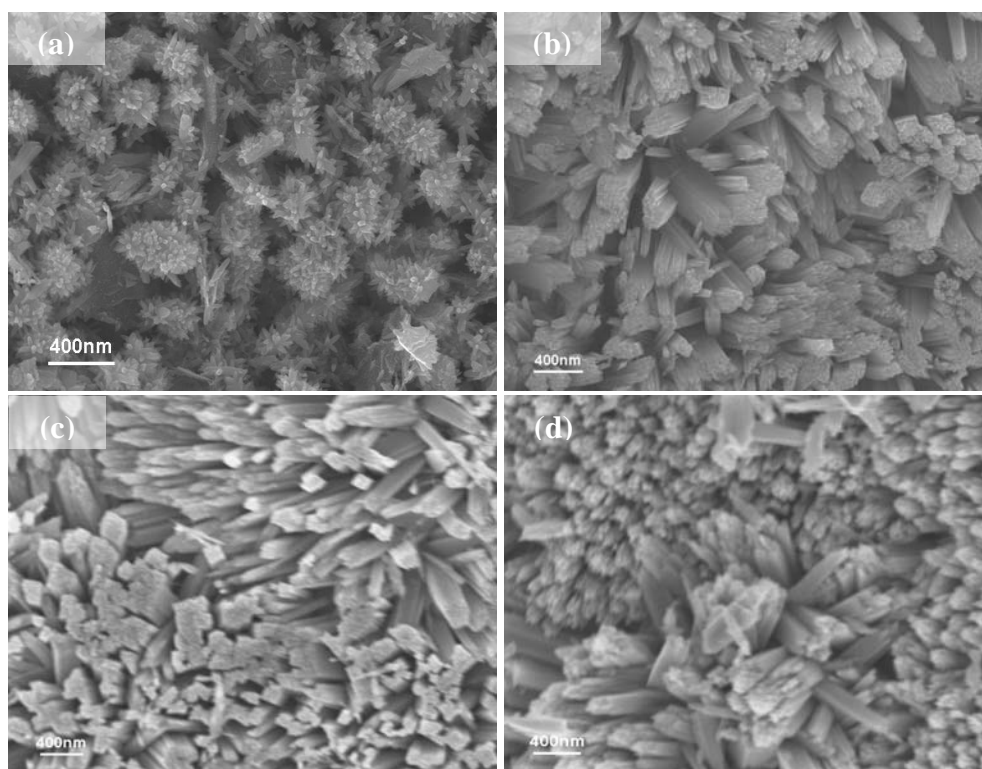


Fig.3.3 SEM images of TiO_2 nanorods/graphene synthesized with different reaction time.

(a) 1h, (b) 4h, (c) 6h, (d) 15h.

reaction at 175°C for 1h are non-uniform aggregates consisting of small particles and short nanoneedles and these aggregates have already begun to form sea urchin type. After hydrothermal reaction for 4h, TiO_2 nanorods are clearly observed as

shown in Fig.3.3b. The morphology of TiO₂ nanorods show less changes when the reaction time is further increased to 6h (Fig.3.3c) and 15h (Fig.3.3d).

3.3.2 Structure and Optical Properties of TiO₂ Nanorods/Graphene

Raman study (Fig.3.4) shows typical Raman spectra for TiO₂ nanorods/graphene composites which were heated for 4h. The strong band around 447cm⁻¹ is attributed to Ti-O-Ti vibration (E_g mode), the other two remarkable bands at 235 and 609cm⁻¹ are assigned to multi-photon process and A_{1g} mode [7]. Two peaks observed at about 1325cm⁻¹(D band) and 1590cm⁻¹ (G band) can be attributed to the graphene templates (see inset in Fig.3.4).

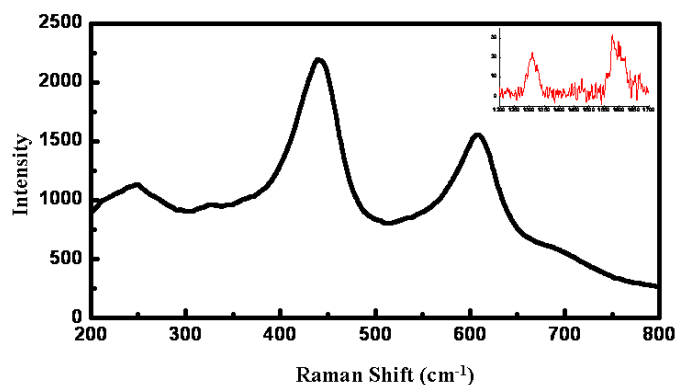


Fig.3.4 Raman spectroscopy of TiO₂ nanorods/graphene

Fig.3.5 shows the Raman spectra of graphene in the nanocomposites with different TiO₂/graphene ratios; we can observe that intensities of both D and G bands increase with the increase of graphene content. The D/G ratio did not show significant difference with respect to graphene content. At this time, the maximum graphene content we used for composites synthesis is around 2mg/0.0075mol TiO₂. Our further research will employ more graphene into the composites. Theoretically, D/G intensity ratio for TiO₂/graphene composites are very similar to that of the bare graphene sheets, indicating that the TiO₂ was grown on the existing defects in the graphene sheets without introducing more defects[4, 8].

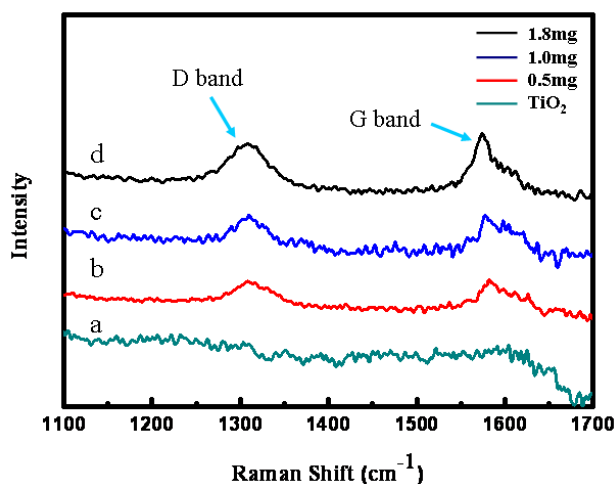


Fig.3.5 Raman Spectra of TiO_2 nanorods/graphene with different graphene content.

(a) bare TiO_2 , (b) 0.5mg, (c) 1.0mg, (d) 1.8mg graphene in composites

Fig.3.6 illustrates Diffusion Reflectance UV spectrum (DRUVS) of pure TiO_2 and TiO_2 /graphene nanocomposites with different graphene contents. The presence of graphene in TiO_2 /graphene composites is responsible for the enhanced adsorption in the visible regions.

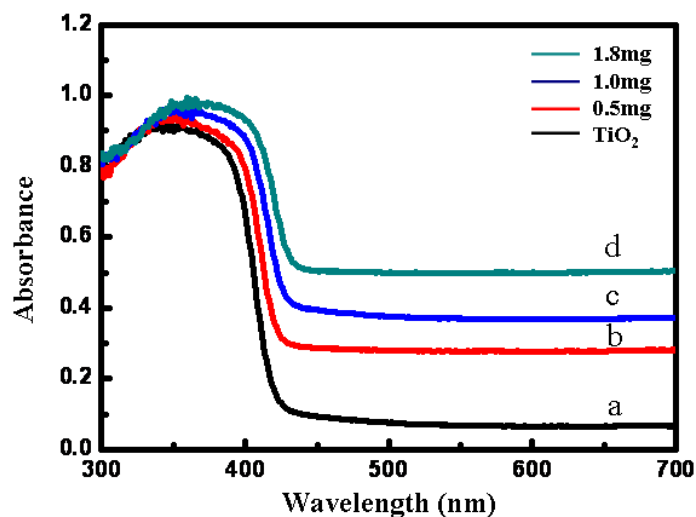


Fig.3.6 Diffusion reflectance UV spectra of pure TiO_2 and TiO_2 /graphene composites with different graphene content. (a) bare TiO_2 , (b) 0.5mg, (c) 1.0mg, (d) 1.8mg graphene

In addition, TiO_2 /graphene composites exhibit red shift of the absorption edge compared to the pure TiO_2 . It can also be observed that this red shift gradually increases with graphene content. This variation of absorption property suggests

strong electronic coupling between TiO_2 and graphene. As is well known, the photocatalytic efficiency of TiO_2 is greatly limited by the relative fast electron-hole recombination, which results in decreased photocatalytic efficiency. The unique electronic property of the graphene sheets and especially the observed strong electronic coupling would help to accept photoexcited electrons to prevent electron-hole recombination. It is believed that a better linkage between graphene and TiO_2 will facilitate electron transfer and result in improved photocatalytic efficiency [4].

3.3.3 Mechanism Study of TiO_2 Nanorods/Graphene Composites

The proposed growth mechanism is illustrated in Fig.3.7. Graphene plays the role of substrate for TiO_2 growth. The fact we got both microsphere assembly and

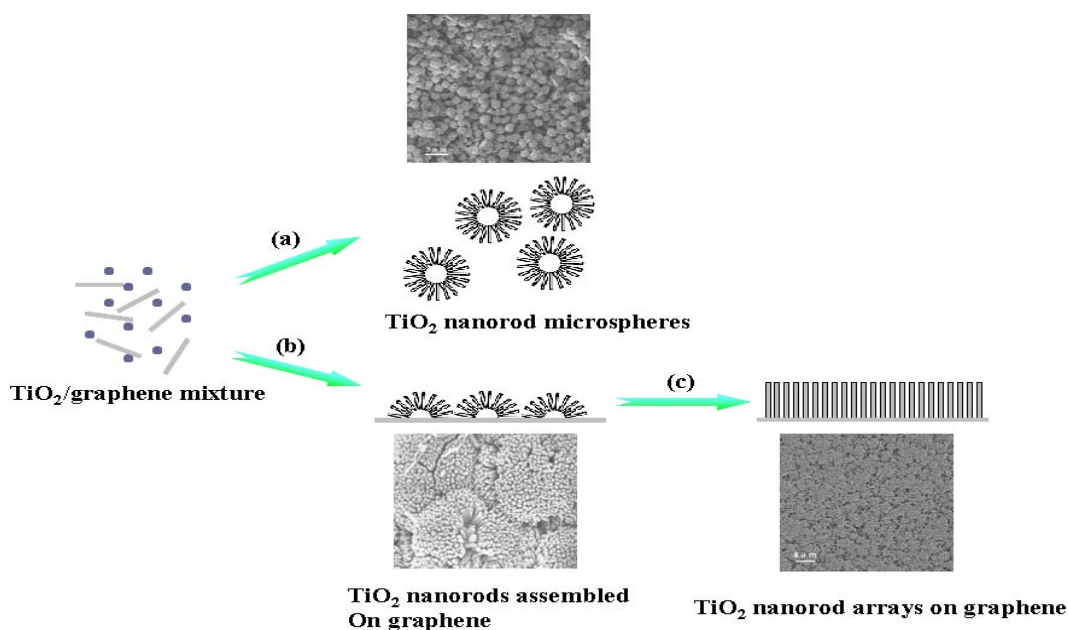
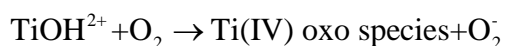
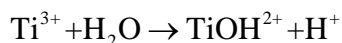


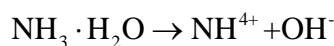
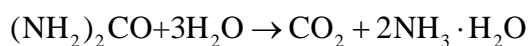
Fig.3.7 Schematic illustration of the formation of 3D hierarchical TiO_2 /graphene nanocomposites and nanorod arrays. Nanorods growth occurred at (a) some spots in bulk solution, (b) nuclei formed on graphene, (c) vertically aligned nanorod arrays were obtained if the density crystal seeds on graphene is high enough.

nanorod array sheets indicates the nucleation of crystal seeds occurred at some spots on graphene as well as in the bulk solution. Subsequent growth takes place to form nanorods along the active facets and self-assemble into microspheres, or bind with each other to form nanorods on graphene, vertically aligned nanorod arrays on graphene due to crowding effect.

The reaction to form TiO_2 is assumed to be:



Ti (IV) oxo species are considered to be an intermediate consisting of dehydrated polymeric Ti(IV) hydroxide [9]. The role of urea is to coordinate Ti^{3+} to form the initial growing nuclei, which directed further heterogeneous nucleation of TiO_2 on specific substrate or bulk solution. Also, urea gradually releases NH_3 to increase the pH values of solution and thus facilitate growth of TiO_2 crystals [9].



In conclusion, we present a facile one-step hydrothermal method to prepare TiO_2 /graphene composites by using TiCl_3 and home-made graphene as starting materials. TiO_2 /graphene nanocomposites have been synthesized elsewhere for photodegradation of organic contaminants [4, 8]. However, so far as is known, TiO_2 in composites are nanoparticles and no research was reported on TiO_2 nanorods based composites. The SEM images show that the resulting products exhibit both urchin-like microsphere assemblies and vertical aligned nanorod arrays. Some key synthesis parameters such as hydrothermal reaction time and graphene content were studied in our experiments. Further optimization will be carried out in order to achieve more comprehensive understanding of the composites formation mechanism. More importantly, the red shift of absorption edge in UV-vis spectra indicates promising enhancement of TiO_2 photocatalytic efficiency in the presence of graphene. Further research will be focused on investigation of photodegradation activity of organic contaminants with our synthesized composites.

References

- [1] Y. H. Ng, I. V. Lightcap, K. Goodwin, M. Matsumura, P. V. Kamat. *J. Phys. Chem. Lett.* 1 (2010) 2222.
- [2] K. Woan, G. Pyrgiotakis, W. Sigmund. *Adv. Mater.* 21 (2009) 2233.
- [3] Y. T. Liang, B. K. Vijayan, K. A. Gray, M. C. Hersam. *Nano Lett.* 11 (2011) 2865.
- [4] K. F. Zhou, Y. H. Zhu, X. L. Yang, X. Jiang, C. Z. Li. *New J. Chem.* 35 (2011) 353.
- [5] L. Liu, J. S. Qian, Y. M. Cui, X. F. Zhou, X. F. Guo, W. P. Ding. *Chem. Commun.* 46 (2010) 2402.
- [6] X. Feng, K. Shankar, O. K. Varghese, M. Paulose, T. J. Latempa, C. A. Grimes. *Nano. Lett.* 8 (2008) 3781.
- [7] H. L. Ma, J. Y. Yang, Y. Dai, Y.B. Zhang, B. Lu, G. H. Ma. *Appl. Surf. Sci.* 253 (2007) 7497.
- [8] H. J. Zhang, P. Xu, G. D. Du, Z. W. Chen, K. Oh, D. Y. Pan, Z. Jiao. *Nano Res.* 4 (2011) 274.
- [9] Y. B. Zhang, X. J. Feng, L. Jiang. *Sci. China Ser B-Chem* 50 (2007) 175.

Conclusion and Future Work

With the completion of this thesis, macro-3D carbon nanotube/metallic wool hierarchical hybrids were synthesized by chemical vapor deposition. The quality of CNTs on metallic wool was improved and acceptable CNT forests were obtained, which are expected to enhance the adherence and contact resistance between CNTs and conducting substrate. Also, an NH_3 sorption system was established to investigate the thermodynamic properties of different adsorbents. Isosters of NH_3 sorption were measured (IS measurement) and the availability of different mathematic models to study NH_3 sorption behavior and capacity were evaluated; we found CNTs have greater potential for NH_3 adsorption than inorganic salt/porous matrices.

The IS measurement is useful for evaluation of adsorptive cooling efficiency. In the future, we are looking forward to establishing an adsorptive cooling device to test the performance (COP) of different solid adsorbents, our CNTs/metallic wool hybrids are expected to enhance the heat transfer and result in better cooling efficiency.

In addition, we successfully synthesized rutile TiO_2 nanorods/graphene composites for photocatalytic applications. Our preliminary study exhibits that the nanocomposites have urchin-like assembly. The energy levels of TiO_2 were tuned in the presence of graphene, with our expectation to enhance the photocatalytic activity towards organic contaminants.

Future study will be focused on the improvement of synthesis condition for more detailed study of the presence of graphene. Photocatalytic studies will also be carried out using our composites. It is believed that further improvements in the structures and photocatalytic performance of TiO_2 /graphene composites are needed to develop practical applications in environmental fields.

Curriculum Vitae

Tao Ma

Date and Place of Birth: Jun. 11, 1983, Hanzhong, China **Email:** uknow83@gmail.com

EDUCATION

Aug. 2009- Dec. 2011 Chemistry Department, Rutgers University(Newark)

Master of Science Degree in Chemistry

GPA: 3.89/4

◆ Dissertation: Macro-3D Carbon Nanotube/metallic Wool Hierarchical Hybrids for Adsorptive Cooling and Novel TiO₂/graphene Composites for Photocatalytic Applications

◆ Supervisors: Prof. Huixin He

Sept. 2006-Jun. 2009 School of Chemistry and Chemical Engineering, Nanjing University

Master of Science Degree in Chemistry

GPA: 87/100

◆ Dissertation: Silicon-based PEG Directed Semiconductor Nanorod Arrays

◆ Supervisors: Prof. Weiping Ding and Associate Prof. Xuefeng Guo

Sept. 2002-Jul. 2006 School of Chemistry and Chemical Engineering, Nanjing University

Bachelor of Science Degree in Chemistry

GPA: 88/100

◆ Dissertation: Synthesis and Characterization of 1D semiconductor ZnO nanostructures

◆ Supervisors: Prof. Weiping Ding and Associate Prof. Xuefeng Guo

RESEARCH EXPERIENCE

◆ CVD growth of CNTs and adsorptive cooling effect study

◆ Investigation for silicon-based PEG directed nanowire arrays

◆ Propene oxidation catalyzed by ferric molybdate nanotubes

◆ PEG directed Microsphere Organization of Nanorods

◆ Catalytic growth of ZnO nanowires through CVD approach

PUBLICATIONS AND PRESENTATIONS

◆ Ferric oxide and ZnFe₂O₄ nanotubes derived from ZnO/FeOx core/shell structures, Min Mo, **Tao Ma**, Xuefeng Guo, Weiping Ding*, *Materials Letters*, **2009**, 63, 2233

◆ Preparation, Characterization, and Properties of Ferric Molybdate Nanotubes for Propene Epoxidation by Air, Li Wang, **Tao Ma**, Wei Sheng, Xuefeng Guo, Weiping Ding*, Yi Chen, *Chinese Journal of Catalysis*, **2009**, 30(8), 711

◆ Nanorods assembly on silicon directed by bonded PEG molecules, **Tao Ma**, Danyu Zhang, Xuefeng Guo, Weiping Ding, *3rd Mesoscopic Chemistry Conference, Nanjing University*, **2009**

TEACHING & WORKING EXPERIENCE

Aug 2009—Dec 2011

Teaching Assistant in Dept. of Chemistry, Rutgers University

Jun 2008—Aug 2008

Summer intern in L'ORÉAL CHINA CO. LTD.

Jan 2007—Jan 2008

Teaching Assistant in Dept. of Chemistry, Nanjing University

HONORS & AWARDS

2007—2009

Outstanding Graduate Student Scholarship, Nanjing University

2006

Outstanding Undergraduate Student Scholarship, Nanjing University

2004—2005

Nanjing University People's Scholarship, 1st in class

2003

Nanjing University People's Scholarship, 2nd in class

PERSONAL SKILLS

Language skills

Fluent in spoken English, good command of professional English

Computer skills

Word, PPT, EXCEL, Photoshop, ChemDraw, Origin, etc.